Received: 27 November 2019 | Revised: 4 May 2020 | Accepted: 7 May 2020

DOI: 10.1111/bre.12468

ORIGINAL ARTICLE

Basin Research | IAS EAGE | WILEY

Interplay of eustatic, tectonic and autogenic controls on a Late Devonian carbonate platform, northern Canning Basin, Australia

Ian J. Ferguson[1] | **Anne-Christine Da Silva**[2] | **Nancy Chow**[1] | **Annette D. George**[3]

[1]Department of Geological Sciences, University of Manitoba, Winnipeg, MB, Canada

[2]Pétrologie Sédimentaire, Université de Liège, Liège, Belgium

[3]School of Earth Sciences, The University of Western Australia, Perth, WA, Australia

Correspondence
Department of Geological Sciences, University of Manitoba, Winnipeg, Manitoba, R3T 2N2, Canada.
Email: nancy.chow@umanitoba.ca

Funding information
Fonds De La Recherche Scientifique - FNRS, Grant/Award Number: FNRS-PDR-T.0051.19; Natural Sciences and Engineering Research Council of Canada, Grant/Award Number: RGPIN-005475-2017

Abstract

Frasnian reef complexes along the northern margin of the Canning Basin in northwestern Australia evolved during rifting of the Fitzroy Trough. Geological investigations of the Frasnian Hull platform, which developed on an active tilted fault-block, reveal significant lateral and vertical facies variations superimposed on prominent metre-scale cyclicity. This study uses numerical analyses of facies and magnetic susceptibility data from three measured sections along the Hull platform to test whether a tectonic signal can be distinguished from eustatic and other signals.

Geostatistical analysis of facies variations reveals an exponential distribution of thin (<3 m) facies, characteristic of stochastic depositional processes. Thick subtidal facies predominate in the Guppy Hills (GH) and southeastern Hull Range (SHR) sections near the hangingwall margin, and thick shallow-subtidal to intertidal facies dominate the Horse Springs drillcore (HD 14) section near the footwall margin. Power and wavelet spectral analyses indicate a strong periodic component; Average Spectral Misfit and spectral optimisation methods confirm the presence of Milankovitch eccentricity signals and suggest the presence of obliquity and precession signals. However, the results also expose strong temporal and spatial variation providing evidence for tectonic control. Spectral analyses show strongest periodicity is recorded in short intervals that are not correlated across the platform and provide evidence of variations in sedimentation rate and hiatuses. Time series for the neighbouring GH and SHR sections show no overall statistical correlation, and Markov analysis indicates weakly ordered vertical facies transitions that do not correlate across the platform. Subtidal to intertidal facies data from HD 14 core suggest that at least 35% of the section is absent, almost obscuring the Milankovitch signal. The results indicate a complex set of controls on deposition on the Hull platform with local tectonic effects having produced spatio-temporal moderation of the underlying eustatic signals and autogenic processes adding a localised stochastic response.

KEYWORDS

Canning Basin, carbonate platform, Frasnian, Late Devonian, magnetic susceptibility, Milankovitch periodicity, tectonic control

1 | INTRODUCTION

Cyclical facies arrangements are common in shallow-marine carbonate successions throughout the Phanerozoic rock record. High-frequency metre-scale cycles, in particular, have been the focus of numerous studies that have attempted to understand the relative influence of eustatic, environmental and tectonic controls (e.g. Bosence et al., 2009; Lehrmann & Goldhammer, 1999; Schlager, 2005; Strasser, 2018). Evidence for Milankovitch rhythms of eccentricity, obliquity and precession has been investigated extensively and provides the basis for a cyclostratigraphic approach to geochronology (e.g. De Vleeschouwer et al., 2017; De Vleeschouwer, Whalen, Day, & Claeys, 2012; Ellwood, Tomkin, et al., 2011; Hilgen et al., 2015; Pas et al., 2018; Tucker & Garland, 2010). However, the record of Milankovitch signals, particularly in shallow-marine successions, is typically complicated by variable sedimentation processes, depositional hiatuses, differential compaction and diagenetic effects (e.g. Eberli, 2013; Hilgen et al., 2015; Kemp, Van Manen, Pollitt, & Burgess, 2016; Martinez, 2018; Meyers, 2019; Pollitt, Burgess, & Wright, 2014; Westphal, Hilgen, & Munnecke, 2010). Tectonic mechanisms, where accommodation is generated by episodic, extensional or strike-slip faulting, have received less attention (e.g. Bosence et al., 2009; De Benedictis, Bosence, & Waltham, 2007; Dorobek, 2008; Sardar Abadi et al., 2014). Although a number of studies have discounted fault movement as a feasible mechanism (Goldhammer, Lehmann, & Dunn, 1993; Koerschner & Read, 1989; Osleger, 1991; Read, Osleger, & Elrick, 1991), more recent work has demonstrated that extensional faults, with metre-scale throws and short-term slippage rates and recurrence times, may generate metre-scale cycles (e.g. Bosence et al., 2009; Tucker & Garland, 2010). The role of autogenic environmental mechanisms, such as tidal-flat island or shoal migration and aggradation that can potentially cause pseudo-periodic repetition, has also been extensively investigated (e.g. Belkhedim et al., 2019; Burgess, Wright, & Emery, 2001; Pratt & James, 1986). In many cases, high-frequency cycles and other stacking patterns are likely the products of the complex interplay between eustatic, autogenic and tectonic mechanisms (e.g. Lehrmann & Goldhammer, 1999; Peterhänsel & Egenhoff, 2008; Tucker & Garland, 2010). Although it is difficult to distinguish unequivocally the signals of each mechanism, quantitative analyses of field and core data and forward stratigraphic modelling provide a basis for analysing the interplay of the various controls (e.g. Burgess, 2006, 2016; De Benedictis et al., 2007; Hill, Wood, Curtis, & Tetzlaff, 2012; Kemp & Van Manen, 2019; Meyers, 2019).

The exhumed Late Devonian reef complexes on the Lennard Shelf of the northern Canning Basin in Australia are widely recognised as being one of the best examples of Late Paleozoic reef complexes (Playford, 1980; Playford, Hocking, & Cockbain, 2009). Givetian to late Frasnian carbonate platforms developed on faulted Precambrian basement blocks during extension of the Fitzroy Trough and are characterised by aggradational and backstepping geometry (George, Trinajstic, & Chow, 2009; Playford et al., 2009; Playton et al., 2016; Southgate, Kennard, Jackson, O'Brien, & Sexton, 1993; Ward, 1999). Metre-scale cyclicity has been described as a characteristic feature of Frasnian platforms in the Canning Basin and broadly interpreted as responses to both tectonic sources and orbitally driven eustatic variations (Brownlaw, 2000; Brownlaw, Hocking, & Jell, 1996; Hocking & Playford, 2000; Playford et al., 2009; Playford, Hurley, Kerans, & Middleton, 1989; Read, 1973). Recent sequence stratigraphic and sedimentological study of an early to middle Frasnian platform, the Hull platform (Figure 1), has demonstrated the importance of synsedimentary tectonics and fault-block rotation in controlling differential subsidence and accommodation and overall platform evolution (Chow, George, Trinajstic, & Chen, 2013; George, Chow, & Trinajstic, 2009). Other Frasnian platforms on the Lennard Shelf also present evidence of strong tectonic control (e.g. Chow, George, & Trinajstic, 2004; Dörling et al., 1996; Ward, 1999).

In this study, magnetic susceptibility (MS) and facies data from the Hull platform are analysed using geostatistical, spectral, correlation and Markov methods in order to evaluate the interplay of global orbital forcing, and local tectonic and autogenic processes on carbonate platform sedimentation. As these various processes all involve recurring, high-frequency changes in accommodation and have overlapping timescales, a multi-method numerical approach is needed to consider prudently the temporal and periodic form of the responses. This approach is enhanced in this study by important spatial-scale information provided by the consideration

Highlights

- Numerical analyses of facies and magnetic susceptibility data identify global and local responses in platform carbonates.
- Evidence for Milankovitch periodicity is provided by spectral, wavelet, Average Spectral Misfit and TimeOpt analyses.
- Spatial and temporal response variations across the carbonate platform indicate tectonic forcing due to fault-block rotation.
- Exceedence probability analysis, low correlation between sections and weak Markov cyclicity indicate autogenic control.

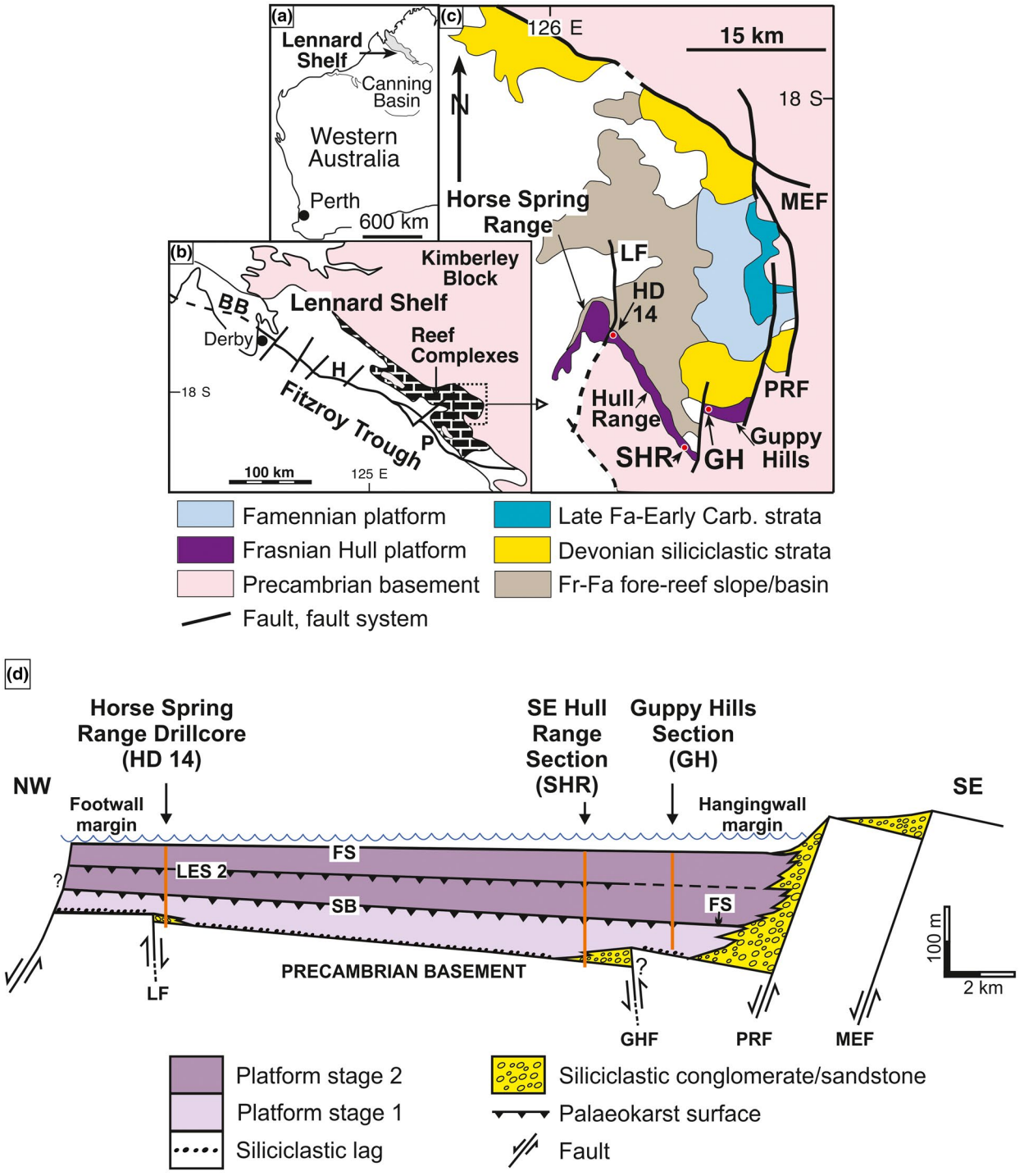

FIGURE 1 (a) Location of the Lennard Shelf in the northern Canning Basin, Western Australia. (b) General distribution of Devonian reef complexes on the Lennard Shelf which is bounded by the Beagle Bay–Harvey–Pinnacle ('BB,' 'H,' 'P') Fault System on the basinward side. (c) Distribution of major geological units in the southeastern Lennard Shelf. BB–H–P, Beagle Bay–Harvey–Pinnacle Fault System; Carb., Carboniferous; Fa, Famennian; Fr, Frasnian; GH, Guppy Hills locality (UTM Map Zone 52K, 198721E/7974566N); HD 14, Horse Spring Range drillcore location (5018E/2610N, dip azimuth vertical); LF, Lindner Fault; MEF, Mount Elma Fault; PRF, Painted Rocks Fault; SHR, SE Hull Range locality (196293E/9970637N). (d) Schematic diagram of the interpreted tectonic setting of the Hull platform which developed on a tilted Precambrian basement block. The major controlling structure was the Mount Elma–Painted Rocks fault system to the east. Modified from Chow et al. (2013). FS, major flooding surface; GHF, Guppy Hills Fault; LES, local exposure surface; SB, subaerial unconformity (sequence boundary)

of measured sections spaced (<16 km apart) across the fault-block platform.

2 | GEOLOGICAL SETTING

The Hull platform is located on the southeastern Lennard Shelf and preserved in the Hull Range, Horse Spring Range and Guppy Hills where it is exposed as a series of ridges with intervening dip slopes and extends approximately 25 km along strike (Figure 1). The ranges are offset or upthrown by late faulting along the Lindner and Guppy Hills faults. Carbonate platform strata, greater than 200 m thick, directly overlie Precambrian granitic-metamorphic basement or siliciclastic conglomerates and sandstones that rest unconformably on basement in this area (Figures 1 and 2). The abundance of deep-subtidal facies dominated by dark-coloured mudstones, shallow-subtidal facies characterised by a variety of skeletal limestones, and intertidal facies distinguished by fenestral peloidal limestones indicate a back-reef depositional setting (Table 1). Measured sections along the Hull platform are divided into facies

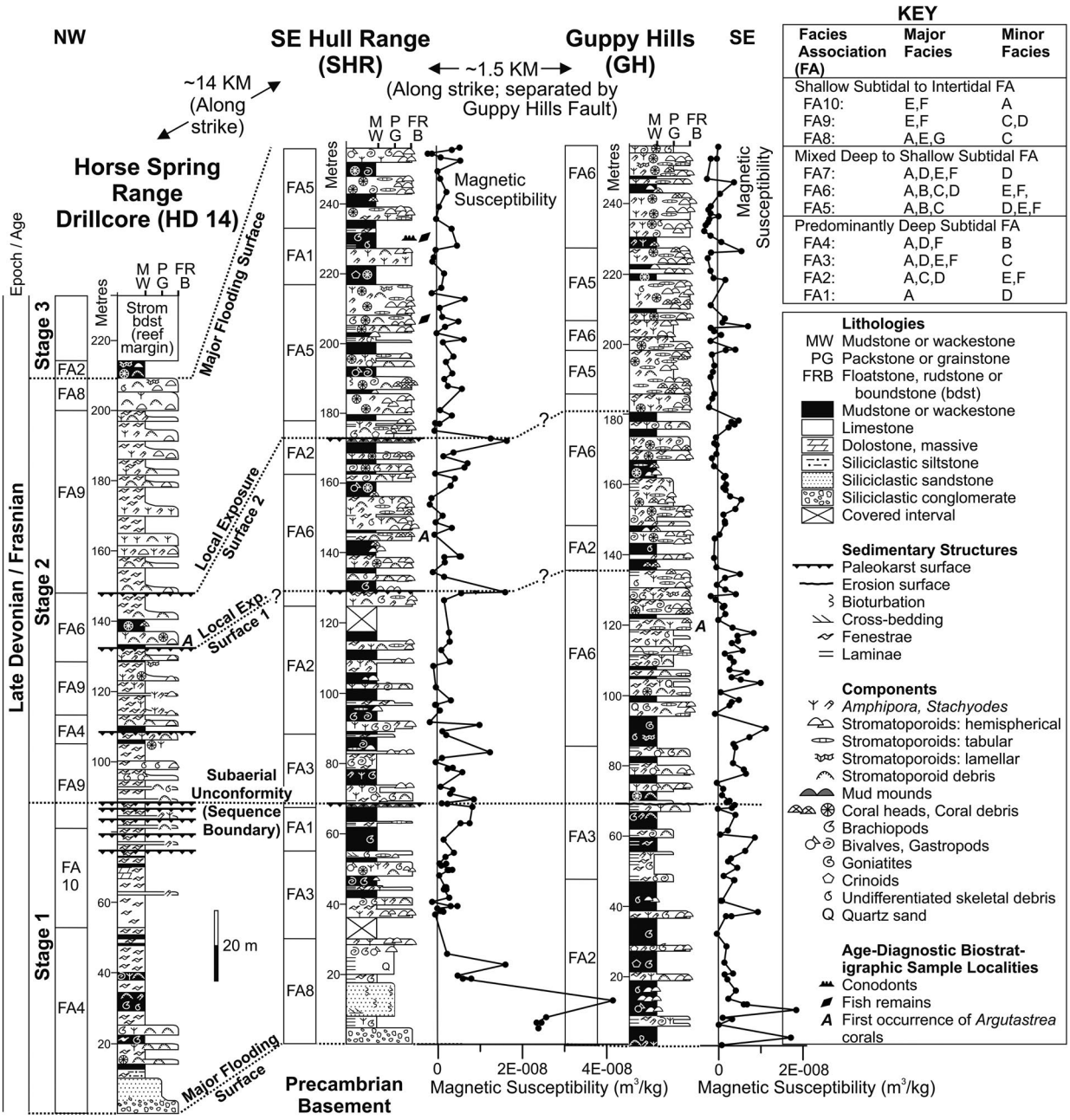

FIGURE 2 Stratigraphic cross-section of the Hull platform showing the measured sections used in this study and plots of MS results. The facies are defined in more detail in Table 1 and the facies associations are defined in the upper right panel. Vertical scale for HD 14 drillcore is given as height above the base of drillcore to be consistent with the outcrop sections

TABLE 1 Summary of facies in the Hull platform

Facies	Thickness	Depositional interpretation
A: Siliciclastic and lime mudstones and associated coral–stromatoporoid–shelly limestones	0.1 to 10.5 m	Deep subtidal; generally low energy with episodic storm events; locally restricted conditions
B: Tabular stromatoporoid bindstones, tabular–hemispherical stromatoporoid boundstones	0.1 to 5 m	Moderate to shallow subtidal, moderate to high energy
C: Irregular–hemispherical stromatoporoid framestones	0.7 to 8 m	Moderate to shallow subtidal, low to moderate energy; bioherms/ biostromes
D: Stromatoporoid rudstones–floatstones ± shelly rudstones–floatstones	0.2 to 4.5 m	Moderate to shallow subtidal, low to high energy; storm-reworked debris
E: Peloidal limestones	0.1 to 2.5 m	Shallow subtidal, low to moderate energy
F: Fenestral limestones	0.1 to 13.7 m	Shallow subtidal to intertidal, low to moderate energy; locally microbial mats
G: Petromict conglomerates/breccias, lithic sandstones	Up to 9.5 m	Deposition during initial transgression; sourced from underlying and adjacent Precambrian crystalline basement

Note: See Chow et al. (2013) for detailed descriptions.

associations based on different constituent facies and/or proportion of facies (Figure 2; see Chow et al., 2013 for detailed descriptions). Facies architecture indicates that initiation and development of the Hull platform on a Precambrian fault block were strongly influenced by syn-depositional normal faulting (George, Chow, et al., 2009). Active fault-block rotation of the half-graben structure and tilting of the hangingwall dip slope generated and maintained wedge-shaped accommodation that deepened towards the southeast (Figure 1d and easternmost stratigraphic column in Figure 2).

Three major depositional stages have been recognised in the Hull platform based on the occurrence of major subaerial exposure surfaces and flooding surfaces (Figures 1d and 2; Chow et al., 2013). Stage 1 represents initial ramp development on the hangingwall dip slope with predominantly deep subtidal conditions. It is characterised by local, basal siliciclastic deposits that are related to small-scale internal faulting (Lindner and Guppy Hills faults) and by an overall deepening-upward carbonate facies pattern. Shallow subtidal to intertidal facies with multiple subaerial exposure surfaces are more common towards the footwall (northwest) margin and deeper subtidal facies predominate near the hangingwall (southeast) margin. Stage 1 is capped by a subaerial unconformity towards the footwall that is correlated with a major flooding surface near the hangingwall; this lateral variation is attributed in part to the fault-block rotation. Stage 2 records major aggradation of the platform and development of reef margins. Thickening of this stage towards the hangingwall and well-developed shallow subtidal to intertidal facies towards the footwall suggest rotation of the fault block and overlying platform. Greater abundance of stromatoporoid framestones and rudstones in the upper part of Stage 2 is considered to represent increasing proximity to the leeward platform margin. The base of Stage 3 is a major flooding surface associated with backstepping of a stromatoporoid–*Renalcis* platform margin due to syn-rift subsidence.

Age determinations of Late Devonian platforms in the Canning Basin are generally challenging due to the paucity of diagnostic fossils. Some workers have relied on the earlier assertion, without clear or new biostratigraphic data, that the Hull platform is Givetian to early Frasnian in age (Hillbun, 2015; Playford et al., 2009; Playton et al., 2016). However, extensive sampling of the Hull Range and Guppy Hills sections has yielded sufficient material to apply conodont, fish and brachiopod biostratigraphy, supported by coral biostratigraphy (Brownlaw & Jell, 2008), and to assign an early to middle Frasnian age to the entire exposed Hull platform (Figure 2; Chow et al., 2013). Based on conodont biostratigraphy, the base of the platform in the Hull Range is as old as Zone 2 and platform facies in the Horse Spring Range are overlain by conodont Zone 6 to Famennian (*marginifera* Zone) fore-reef slope facies (Chow et al., 2013; Klapper, 2007). Using the Devonian timescale compiled by Becker, Gradstein, and Hammer (2012) and the earlier information of Kaufmann (2006), the time represented by the Hull platform as it is currently exposed is approximately 2.5 Myr.

3 | STUDY LOCATIONS AND FACIES DATA

This study is based on three measured sections across the Hull platform. The HD 14 diamond drillcore (238 m thick) from the Horse Spring Range provides the section most proximal to the footwall (northwest) margin of the tilted fault block (Figure 1). The upper 35 m of this core was excluded from the numerical analysis in this study because no corresponding interval is present in the other two sections analysed. The outcrop sections from the Hull Range (SHR section; 257 m

thick) and Guppy Hills (GH section; 256 m thick) are located near the hangingwall (southeast) margin (Figure 1).

Seven major facies (A to G; Table 1) are recorded sufficiently frequently in the measured sections to be suitable for direct use in numerical analyses and they represent significant variations in depositional processes and conditions that are useful for interpretation of cyclical patterns. In order to achieve greater statistical reliability for some of the geostatistical analyses, the carbonate facies were combined into pairs based on the textural and compositional similarities and interpreted depositional origin. The facies pairs are deep to moderate/shallow subtidal mudstones (A–B), moderate to shallow subtidal stromatoporoid limestones (C–D) and shallow subtidal to intertidal peloidal/fenestral limestones (E–F). The distribution of the facies pairs in the three measured sections is shown in Figure 3. Siliciclastic facies G is retained as a single class. The clustering of sub-units into broader classifications for geostatistical analysis has also been applied in a number of previous studies (e.g. Chen & Hiscott, 1999b).

4 | MS DATA

4.1 | MS measurements

MS intensity of Devonian carbonate rocks provides a proxy for base-level changes during platform evolution based on detrital sediment input during lowered base level (e.g. Da Silva & Boulvain, 2006; Da Silva, Mabille, & Boulvain, 2009; Da Silva, Potma, et al., 2009; Da Silva et al., 2015; De Vleeschouwer et al., 2013; Ellwood, Crick, El Hassani, Benoist, & Young, 2000; Riquier, Averbuch, Devleeschouwer, & Tribovillard, 2010; Śliwiński, Whalen, Meyer, & Majs, 2012; Whalen & Day, 2010). The recognition of Milankovitch-scale cyclicity in MS values has enabled cyclostratigraphic calibration of portions of the Devonian timescale (Da Silva et al., 2013, 2016; De Vleeschouwer et al., 2012; Ellwood, Tompkin, et al., 2011; García-Alcalde, Ellwood, Soto, Truyóls-Massoni, & Tomkin, 2012).

MS analysis of the SHR and GH sections was undertaken on samples collected every one to two metres, except through recessive-weathered intervals, such as in the lower 37 m of the SHR section (Figure 2). All facies were sampled, except in recessive mudstone-dominated intervals where only exposed skeletal limestone beds could be sampled, and in coral or stromatoporoid boundstone facies, where skeletal muddy or peloidal matrix was sampled. A total of 127 samples for the SHR section and a total of 142 samples for the GH section were analysed.

MS measurements were done using a KLY-3S Kappabridge (AGICO) at the University of Liège (Belgium). The precision of the device in terms of volume susceptibility is 3×10^{-8} SI (AGICO, 2003). Results are reported here in terms of mass-normalised MS expressed in m^3/kg; each data point is the average of three measurements. The sample mass was weighed with a precision of 0.01 g.

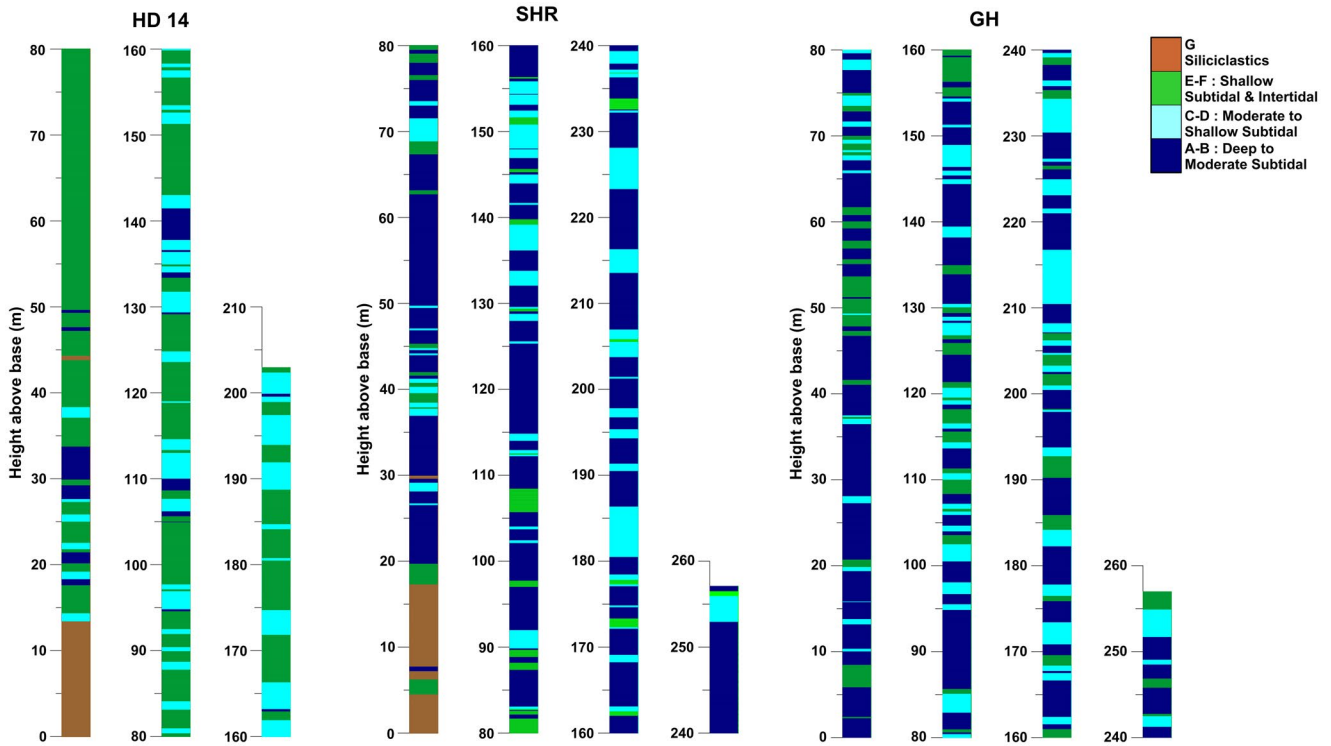

FIGURE 3 Distribution of facies pairs for the three measured sections.

4.2 | MS results

MS values for the SHR section range from -2.15×10^{-9} to 4.15×10^{-8} m^3/kg (mean of 3.53×10^{-9} m^3/kg; median of 1.91×10^{-9} m^3/kg) and the values for the GH section range from -3.44×10^{-9} to 1.84×10^{-8} m^3/kg (mean of 1.94×10^{-9} m^3/kg; median of 1.50×10^{-9} m^3/kg) (Figure 2). A large proportion of the MS values is negative: 21% for SHR and 32% for GH. The averaged results show that the MS values for the SHR section are slightly higher than those for the GH section, although the median value for the two sections differs by only about 20%.

MS data from the SHR and GH sections show an upward decreasing trend over most of each section and a number of peaks (Figure 2). MS values are higher in the basal strata of these sections in the siliciclastic facies. Peaks also occur in the lime mudstone or wackestone units at the interpreted location of two local exposure surfaces. In the SHR section, these peaks have a magnitude of ~2×10^{-8} m^3/kg and are the largest signals in the carbonate part of the section. In the GH section, the corresponding peaks have a magnitude of ~1×10^{-8} m^3/kg.

The negative MS values between the peak values in the SHR and GH sections (Figure 2) indicate that background magnetisation is controlled by diamagnetic matrix minerals (e.g. calcite) with minimal contribution from paramagnetic, antiferromagnetic and ferromagnetic minerals. Based on hysteresis and high field analysis, the peaks in the MS are interpreted to be controlled by the paramagnetic component, which in platform carbonate successions is typically dominated by clay minerals and pyrite (e.g. Ellwood et al., 2000; Ellwood et al., 2013; Königshof et al., 2015). The origin of these paramagnetic minerals is typically attributed to a primary detrital origin (Da Silva et al., 2016; Königshof et al., 2015).

5 | GEOSTATISTICAL ANALYSIS

5.1 | Qualitative examination of the facies pair distribution

Visual inspection of the distribution of facies pairs (A–B, C–D, E–F and G) in the HD 14, SHR and GH sections (Figures 2 and 3) reveals notable differences within individual sections and between the sections. For example in HD 14, facies pair A–B occurs in only a few short (<20 m) intervals (Figure 3). In the SHR and GH sections, there are no thick beds (>1 m) of facies pair C–D in the lower 70 m of the sections (Figure 3). The measured sections display stronger alternations over intervals which vary between the sections. For example in the HD 14 section, the interval between 80 and 95 m has an alternating succession of thicker facies pair E–F units and thinner facies pair C–D units with a repetition length-scale of about 2.5 m (Figure 3). The upper 50 m contains alternating thicker beds of facies pairs C–D and E–F with a repetition length-scale of about 5 m. In the SH section, between 180 and 240 m, a series of relatively thick (3 to 5 m) facies pair C–D is separated by facies pair A–B with a repetition length-scale of 8 to 10 m (Figure 3).

5.2 | Statistical distribution of facies pair thickness

Statistical analysis of stratal thickness provides important information on underlying sedimentological processes. In a purely random or Poisson process, the probability of occurrence or thickness of a particular bed is independent of the preceding beds, and the stratal thickness distribution is defined by an exponential or gamma function (e.g. Chen & Hiscott, 1999a, 1999b; Drummond & Coates, 2000; Wilkinson, Drummond, Diedrich, & Rothman, 1999). In contrast, the thickness of beds deposited in a strongly periodic process may be clustered around a particular value, producing a probability distribution with a clear peak.

In this study histogram analysis was used to provide characterisation of the individual and combined facies pair thickness distribution in each of the HD 14, SHR and GH sections (Figure 4). An exponential function was fitted to the frequency distribution results to compare the data with the corresponding theoretical distribution. For all data sets, the distribution of the facies pair thickness is strongly positively skewed with an approximately exponential form. The higher resolution (smaller bin) results available for the combined facies pair data show a relative decrease in the abundance for the thinnest beds which is characteristic of a gamma distribution (e.g. Drummond & Coates, 2000). The frequency of occurrence of the thickest beds exceeds the theoretical value for an exponential distribution and contributes to the strong positive skew. The absence of narrow peaks in the facies thickness histograms for each measured section supports the absence of temporally uniform periodicity throughout the measured sections.

The facies pair thickness is largest in the HD 14 section (with a mean value of 2.2 m) and smallest in the GH section (with a mean of 1.4 m). The statistical distribution for the facies pairs in the SHR and GH sections is similar, with a peak at <0.5 m thickness and most facies pairs <2.5 m thick (Figure 4). In these two sections, facies pair A—B tends to form the thickest beds with a distribution between 0.1 and 5 m and a mean interval thickness of ~2 m, whereas the mean thickness of facies pairs C–D and E–F is about 1 m. In the HD 14 section, the facies pair E–F forms the thickest beds with many facies pairs >3 m thick (Figure 4). Facies pair E–F has a mean thickness of 3.2 m, in contrast to 1.1 and 1.3 m for facies pair A–B and C–D, respectively.

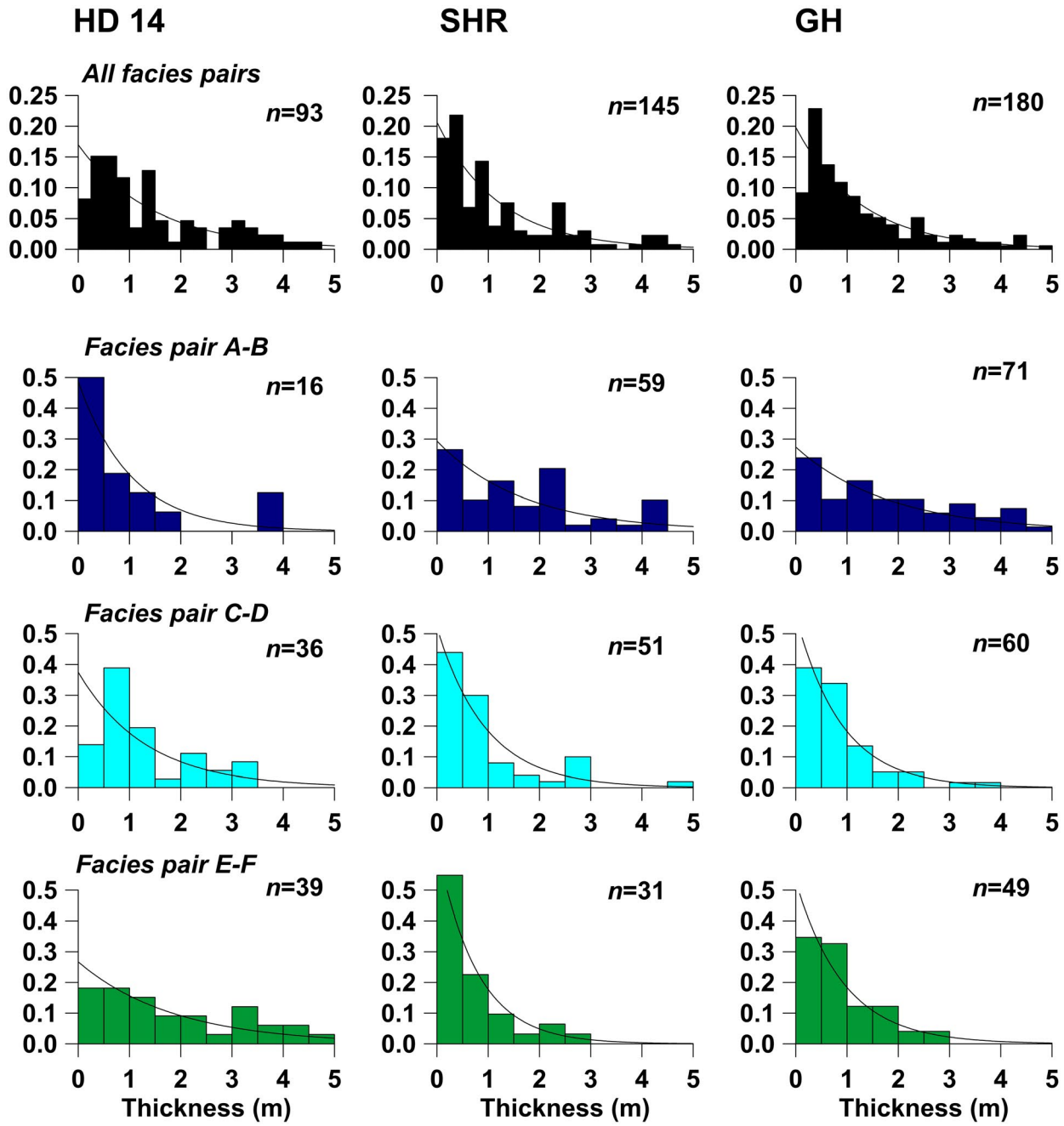

FIGURE 4 Histograms showing the relative frequency of occurrence of units of different thicknesses. The upper panel shows results for all of the facies pairs (using 20 bins and 0.25 m intervals) and the lower three panels show the results for individual facies pairs (using 10 bins and 0.5 m intervals). Values exceeding 5 m have been omitted from the plots. The curve shown on each panel is the best-fitting exponential distribution. The colour coding of facies pairs is the same as in Figure 3

Cumulative frequency plots of stratal thickness provide additional information on statistical thickness distributions. These plots were constructed for the Hull platform data using the probability exceedence parameterisation (Chen & Hiscott, 1999a; Drummond, 1999; Drummond & Coates, 2000; Rothman & Grotzinger, 1995; Wilkinson et al., 1999; Wilkinson, Drummond, Rothman, & Diedrich, 1997) (Figure 5). On a log-linear exceedence plot, exponentially distributed data plot as a straight line (Drummond, 1999). The results for the HD 14, SHR and GH sections show facies pairs, less than 3 to 6 m thick, are distributed approximately exponentially and can be fitted closely by a straight line on log-linear plots (Figure 5a). Thicker facies pairs follow a different exponential distribution with a negative exponential constant (the slope of the line in Figure 5a) that is smaller than that of the thinner facies pairs. This difference indicates that the thicker facies pairs are present in a greater abundance than would be expected for a fully random process.

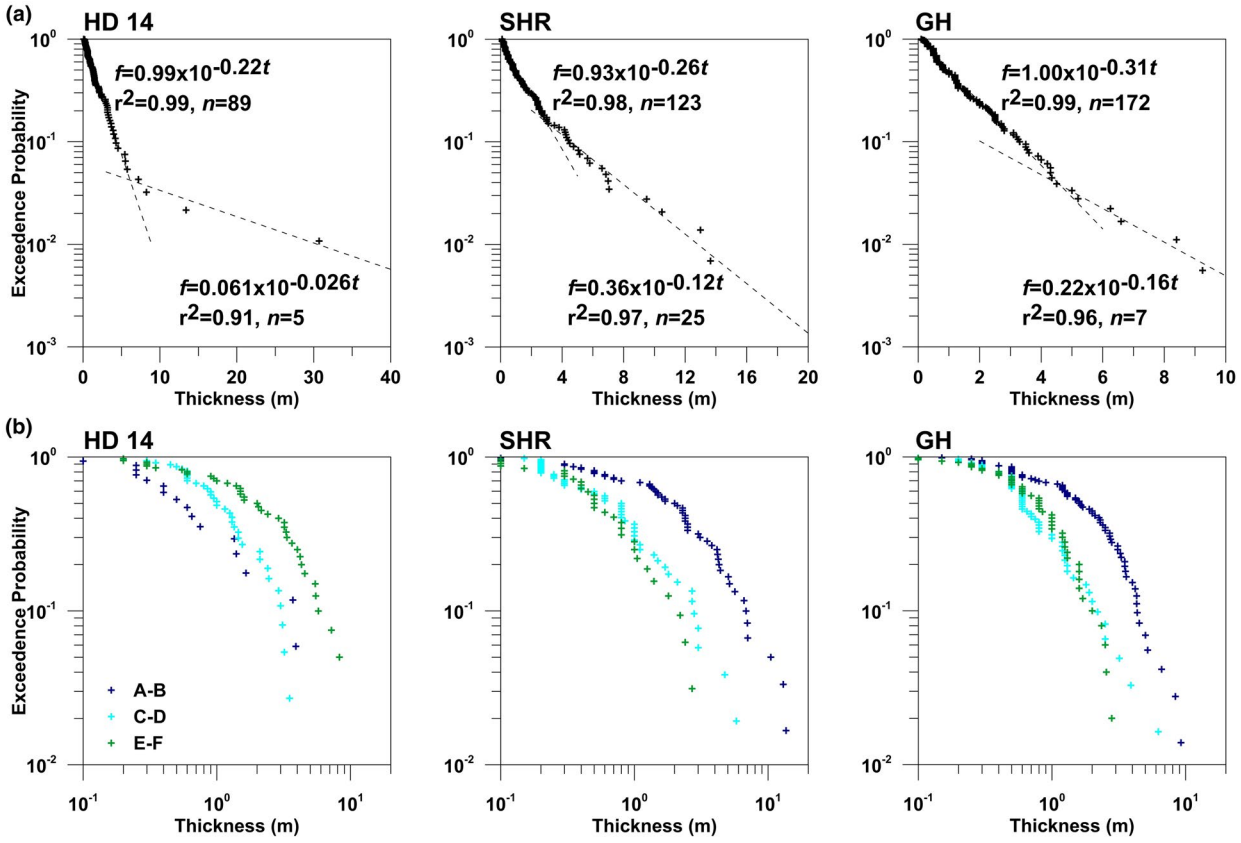

FIGURE 5 Exceedence probability results for the three Hull platform sections. (a) Combined results for all facies pairs using a linear probability axis. Plots show the probability of the strata exceeding a particular thickness. A straight line fit indicates the data conform to a Poisson model of random occurrence. The equations define the negative exponential functions fitted to the data and the squared correlation coefficients. The fits were done after log transformation of the data. (b) Results for individual facies pairs using a logarithmic probability axis. Straight line segments correspond to power-law relationships, that is, to a particular fractal dimension

On a log-log plot of exceedence versus thickness, data lying on a linear trend define a power-law relation and are interpreted as representing a fractal or scale-invariant process (e.g. Rothman & Grotzinger, 1995). The slope of the linear trend defines the probability of beds of particular thickness: a data set with a lower slope represents strata that, at a given probability of occurrence, are thicker than strata from a data set with a higher slope (e.g. Rankey, 2002). When plotted using the log-log scaling the data from the three Hull platform sections have a curved form (Figure 5b) confirming that the data conform to an exponential distribution rather than a power-law distribution (Drummond, 1999). The results are consistent with a Poisson process rather than a scale-invariant fractal process.

Variations between the three facies pairs are also apparent in the exceedence plot (Figure 5). For HD 14, the progressively higher slopes between facies pairs E–F, C–D and A–B indicate that at a given probability of occurrence, the thickness of E–F is greater than for C–D and in turn for A–B. For the SHR and GH sections, the lowest slopes are observed for A–B indicating that for a given probability of occurrence, the thickness of A–B is greater than for C–D and E–F. In other words, for all thickness scales, facies pair E–F on average forms the thickest stratal units in the HD 14 section, whereas facies pair A–B on average forms the thickest stratal units in the SHR and GH sections.

5.3 | Evolutionary trends in facies pair thickness

Further information on depositional processes can be derived from methods that consider the evolutionary variation of the sedimentary succession. A number of studies have demonstrated that a sedimentary data set may exhibit apparently random characteristics yet still have a high degree of ordering (e.g. Rankey, 2002) affecting the long-term evolutionary response. Fischer plots relate the cumulative deviation of cycle thickness from mean cycle thickness to cycle number and are useful for examining long-term evolutionary trends (e.g. Chen, Tucker, Jiang, & Zhu, 2001; Fischer, 1964; Koerschner & Read, 1989; McLean & Mountjoy, 1994; Tucker & Garland, 2010; Wilkinson et al., 1999). They are commonly interpreted within a sequence stratigraphic framework with positive-sloped parts of the curves (cycle thickness consistently higher than the mean value) corresponding to

transgressive phases and negative-sloped parts (cycle thickness consistently lower than the mean value) corresponding to regressive phases. Minima and maxima represent lowstands and maximum flooding surfaces, respectively.

Facies thickness data from the Hull platform sections were examined using a cumulative thickness approach similar to a Fischer plot analysis with the cumulative facies-pair thickness deviations plotted against stratigraphic thickness. All three sections exhibit a long-term trend of decreased facies-pair thickness over about 150 m length (overall downward slope in Figure 6a), on which is superimposed a series of irregular peaks separated by 20 to 50 m. The longer trends seen in the cumulative thickness deviation plots show excellent agreement with the longer trends in Fischer plots for the GH section determined by Brownlaw et al. (1996). Comparison of the intermediate-term, 20–50 m, trends with the corresponding facies pairs that are present (shown on the bar beneath each plot) indicates that upward trends are caused mainly by thicker facies pair E–F in the HD 14 section and by thicker facies pair A–B in the SHR and GH sections. There are no obvious consistent correlations of these intermediate-term features between the three sections or with key stratal surfaces, such as the subaerial unconformity and local exposure surfaces.

A component of the irregularity in the cumulative thickness plots for the Hull platform sections is probably due to differential compaction of the different facies. Hence estimated decompaction factors, based on the likely depth of burial and published compaction estimates (Table 2; Doglioni & Goldhammer, 1988; Goldhammer, 1997), were applied and the results were resampled at 5 cm intervals to provide decompacted data sets (Figure 6b). The decompacted results, particularly those for the SHR section, show the intermediate-scale variations as a prominent pattern of peaks separated by 40–50 m. These peaks are asymmetrical, showing a relatively gradual increase in cumulative facies-pair thickness followed by a relatively rapid decrease.

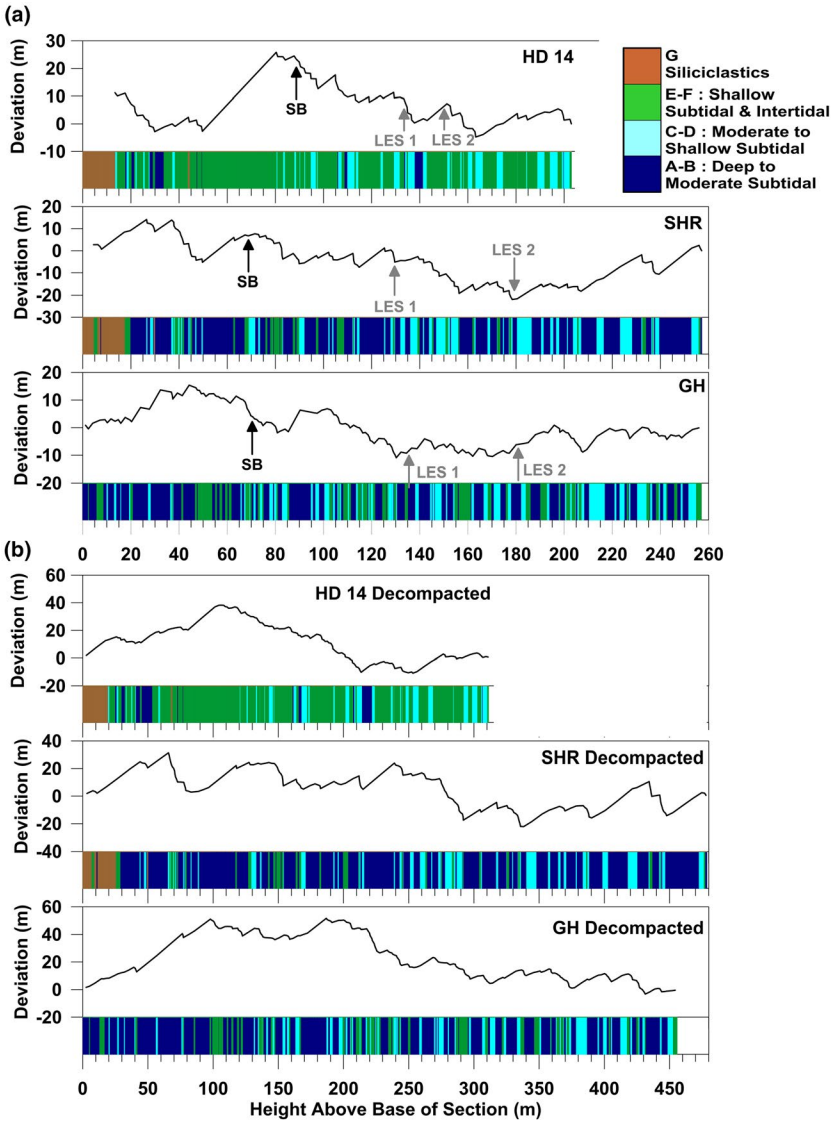

FIGURE 6 Cumulative facies-thickness deviation plots (Fischer plots). (a) Results for observed facies-pair thicknesses. Black arrows show the interpreted location of the subaerial unconformity (sequence boundary, SB) and grey arrows show the interpreted location of local exposure surfaces (LES). (b) Results for decompacted facies-pair thicknesses. The plots show the deviation between the cumulative facies-pair thickness and a value based on the mean facies-pair thickness plotted at the height of the base of each facies pair unit above the base of the measured section. The bar beneath each set of results shows the facies pairs

TABLE 2 Compaction factors for Hull platform facies

Component	Compaction factor	Source
Individual facies (refer to Table 1)		
A: Siliciclastic and lime mudstones and associated coral–stromatoporoid–shelly limestones	0.55	Goldhammer (1997)
B: Tabular stromatoporoid bindstones, tabular–hemispherical stromatoporoid boundstones	0.30	Goldhammer (1997)
C: Irregular–hemispherical stromatoporoid framestones	0.20	Goldhammer (1997)
D: Stromatoporoid rudstones–floatstones ± shelly rudstones–floatstones	0.30	Goldhammer (1997)
E: Peloidal limestones	0.30	Goldhammer (1997)
F: Fenestral limestones	0.20	Goldhammer (1997)
G: Petromict conglomerates/breccias, lithic sandstones	0.30	Doglioni and Goldhammer (1988)
Average for section after the decompaction of individual facies		
HD 14	0.35	
SHR	0.46	
GH	0.44	

6 | SPECTRAL ANALYSIS

6.1 | Spectral and wavelet methods

Examination of periodic signals, such as those associated with Milankovitch cyclicity, in a time series requires the application of spectral methods (e.g. Hinnov, 2000; Schwarzacher, 2000; Weedon, 2003). Weedon (2003) provides a comprehensive description of methods for determining the power spectra of sedimentary sections. The wavelength of the shortest cycles that can be resolved in spectral analyses, referred to as the Nyquist wavelength, depends on the sampling interval. The thinnest facies units in the observed data have a thickness of 5 cm corresponding to a Nyquist wavelength of 10 cm. The observed MS data have an average sampling interval of about 1 m corresponding to a Nyquist wavelength of 2 m.

In the present study, spectral analyses were done on the observed (compacted) and decompacted thickness of individual facies units (A to G) and facies pairs (A–B, C–D, E–F) from each measured section, as well as different segments of the sections. Facies were coded using a numerical value of 1 to 7 for facies A to G, respectively, in decreasing order of interpreted depositional water depth. Additional analyses were done in which individual facies pairs were coded as binary responses corresponding to the presence or absence of the pairs and the results of these analyses are provided in the Supporting Information. In order to calculate spectra for the MS results, the irregularly spaced data were linearly interpolated prior to analysis. For the decompacted sections, the position of each measurement in a particular bed was tracked through the decompaction process, then converted into height above the decompacted section base, and finally, the results were linearly interpolated. MS spectra were examined using both the absolute MS values and the logarithm of the absolute MS. Similar zones of periodicity are seen in both sets of results but the log results show features more clearly and will be presented here.

Power spectra were estimated using Walsh, Welch, and multi-taper method (MTM) algorithms (see Supporting Information for details of these methods). In order to better understand the results of analyses done in this study, the methods were applied to synthetic data sets representing incompletely recorded periodic data (refer to Supporting Information). The results show that for facies data similar to those analysed in the present study, MTM power spectra provide the superior estimate and permit better interpretation than the other spectra. Therefore, only MTM spectra are examined in the following sections. The MTM computations were done using the Strati-Signal® software developed by Ndiaye (2007a, 2007b) and the significance of spectral peaks was examined in terms of the deviation from a robustly fitted background red spectrum at 90% and 95% confidence levels.

Wavelet transformation was used to examine the non-stationarity in the spectral results (e.g. Boulila et al., 2014; De Vleeschouwer et al., 2014; Machlus, Olsen, Christie-Blick, & Hemming, 2008; Prokoph & Agterberg, 1999; Weedon, 2003). This analysis was based on a Morlet wavelet and was done using the Strati-Signal® software

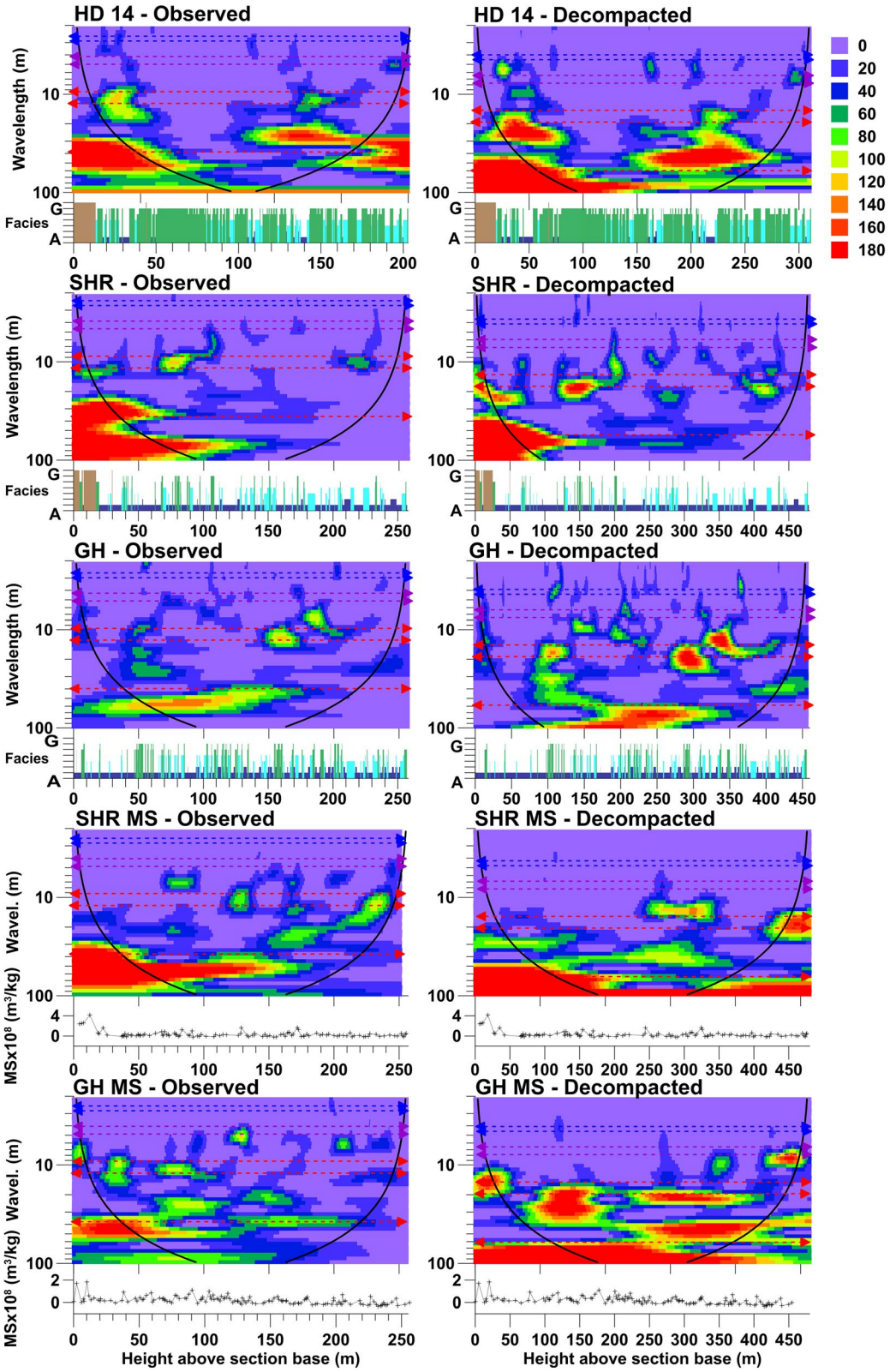

(Ndiaye, 2007a, 2007b). Additional wavelet analyses were also done on the facies and facies thickness data as a function of facies stratal number (ordinal position of each facies in the succession making up the measured section). The results are presented in the Supporting Information.

6.2 | Spectra of facies data

Representative results from the many tens of spectra produced, using wavelet transform and MTM power spectral methods, are presented in Figures 7 and 8. Corresponding

FIGURE 7 Wavelet spectra for the observed and decompacted facies data and magnetic susceptibility (MS) data for each measured section. The contoured spectra are dimensionless. The black curves define the cone of influence; in the region between the curves the wavelet functions do not intersect either the start or end of the data series. Dashed lines show the calculated position of Milankovitch signals assuming an average sedimentation rate of 0.1 m/kyr and for the decompacted sections assuming the average decompaction factor. Red dashed lines show the eccentricity cycles at 404, 124 and 95 kyr; purple dashed lines show the obliquity cycles at 39 and 32 kyr; and blue dashed lines show the precession cycles at 20 and 17 kyr. The bar graph beneath each facies spectrum shows the facies variation with the bar height showing the individual facies from A to G and the colour coding showing the facies pair or facies: dark blue = A–B, light blue = C–D, green = E–F, and brown = G. The graph beneath each MS spectrum shows the original results as points and the linearly interpolated data as a grey line

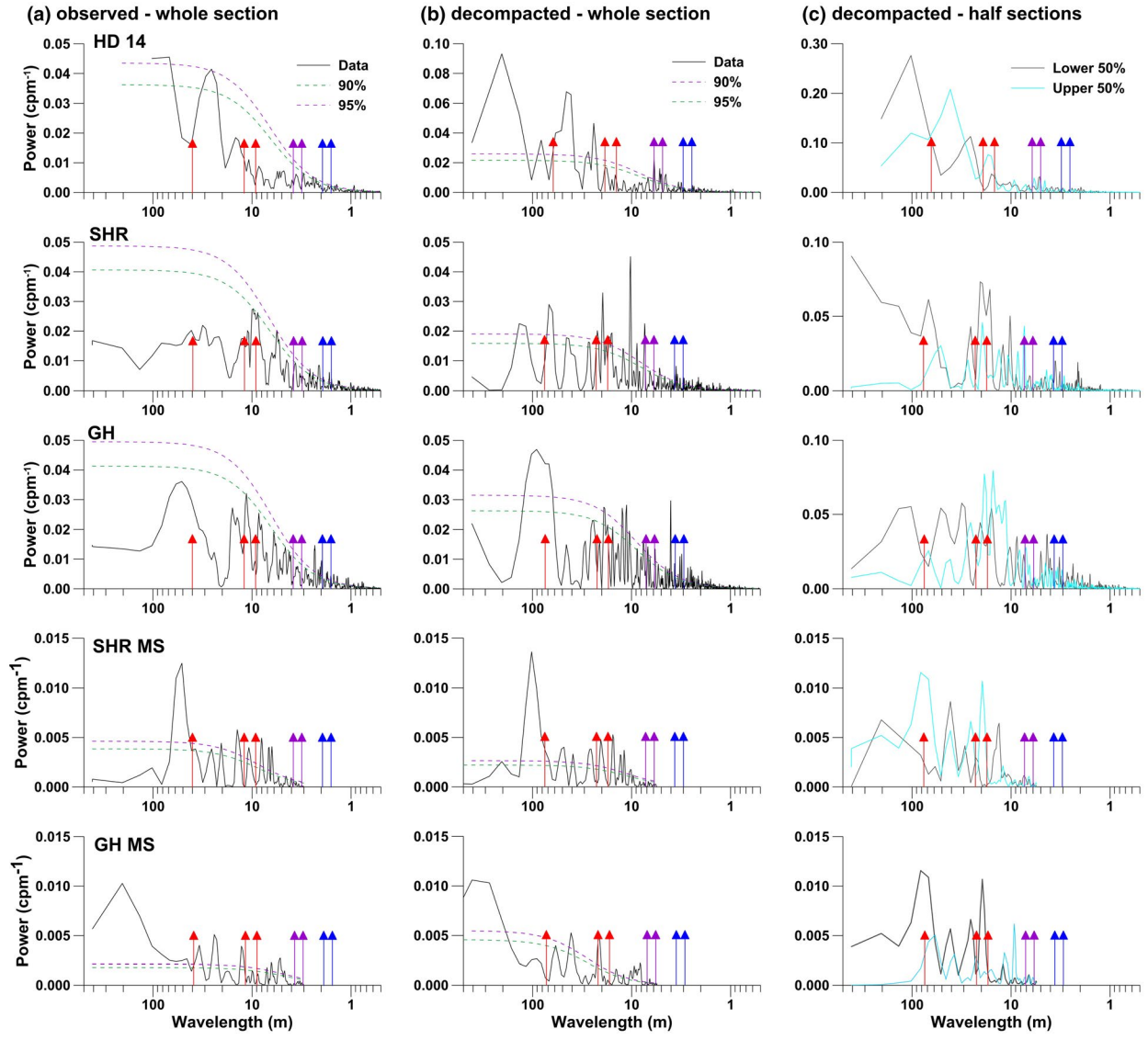

FIGURE 8 Power spectra of facies and log MS data for (a) observed sections, (b) decompacted sections, and (c) decompacted half-sections. Results are multi-taper method (MTM) spectra calculated using Strati-Signal® and 90% (green) and 95% (purple) confidence limits. Facies results were obtained using time-frequency resolution of 4 and 8 tapers and MS using time-frequency resolution of 2 and 5 tapers. Confidence limits are for background red spectra defined robustly in log-space. Red arrows show eccentricity cycles at 404, 124 and 95 kyr; purple arrows show obliquity cycles at 39 and 32 kyr; and blue arrows show precession cycles at 20 and 17 kyr. For the observed data the positioning of the Milankovitch signals is based on the average sedimentation rate of 0.1 m/kyr. For the decompacted data, the positioning is based on the average sedimentation rate adjusted for the average decompaction factor

MTM and wavelet power spectra show periodicity at similar wavelengths (compare Figures 7 and 8).

Components of the enhanced periodicity shown by the wavelet and power spectral results are as follows.

1. 8–30 m wavelengths. All three measured sections show evidence of enhanced periodicity in the wavelength range of 8 to 15 m in the observed data (Figure 8a) and 16–30 m in the decompacted data (Figure 8b). Wavelet results (Figure 7) show this enhanced periodicity does not correspond to a persistent narrow-band signal but instead occurs in patches of relatively broad-band signal (wavelengths varying by a factor of 2 or more) in lengths of the section of less than 60 m. A component of this variation may be due to modulation but some patches exhibit a change in wavelength along the section, indicating the occurrence of irregular sedimentation. The wavelet spectra also show strong differences between the sections. Comparison of the wavelet response with the facies logs of the measured sections (Figure 2) reveals that the patches of enhanced periodic signal are associated with periods of increased facies variability, with all three facies pairs present in those parts of the section, whereas the gaps with less periodic signal are dominated by a single facies pair (E–F in HD 14; A–B in SHR and GH).
2. 10 m wavelengths. The decompacted facies data show evidence for increased periodicity at 10 m wavelength in the SHR section (Figure 7). These signals are defined in seven to ten short zones that span the section but in combination form < 25% of the total data in the section. Spectral results for the GH section also exhibit a statistically significant signal between 10 and 15 m wavelength but the HD 14 results have low magnitude in this wavelength range.
3. <10 m wavelengths. Evidence for weak periodicity at short wavelengths is provided by peaks at 5–6 m wavelength in the decompacted facies spectrum for HD 14 and by peaks at 3–4 m wavelength in the SHR and GH spectra (Figure 8b). The position of these pulses is not correlated between the sections (Figure 7) but the spectra for the upper and lower halves of each section have peaks at similar, but not the same, wavelengths (Figure 8c). Stratal wavelet analysis (see Supporting Information) supports the interpretation of weak periodicity and provides evidence of both amplitude and frequency modulation of the signals.

6.3 | Spectra of MS data

For the MS data, the strength of the periodic responses and the statistical significance of the spectral peaks increase significantly with decompaction (Figures 7 and 8). The SHR and GH MS wavelet responses indicate the presence of narrow-band responses at 40–50 m wavelengths in the observed data and 60–80 m in the decompacted data (Figure 7). These signals persist over much of the record length but exhibit variation in magnitude. At shorter wavelengths, MTM spectra for both SHR and GH data sets exhibit enhanced signal in broad bands centred on about 6 m and 13 m in the observed data and 10 m and 22 m in the decompacted data.

Overall, there is a minimal correlation of periodic signals in the wavelet responses for MS and facies in the SHR and GH sections (Figure 7). Signal peaks in particular wavelength bands occur at different positions in the facies and MS responses. However, long-wavelength signals tend to be stronger for both the facies and MS data in the lower half of each section.

7 | CORRELATION AND MARKOV ANALYSIS

7.1 | Correlation and Markov analysis methods

Correlation analyses are well suited for analysing data containing transient, non-periodic signals. Autocorrelation indicates the self-similarity of a data series at different time-lags and crosscorrelation analyses the similarity of two data series. Autocorrelation and crosscorrelation results were determined for the decompacted facies and MS data using Strati-Signal® software (Ndiaye, 2007a, 2007b). For the autocorrelations, this software provides an estimate of the standard error on the result, and for the crosscorrelations it provides both confidence limits on a statistically significant correlation and an estimate of the equivalent correlation function for white noise.

The shape of the autocorrelation function provides a measure of the memory of the system. For a first-order Markov process, in which the probability of a particular stratal unit being deposited depends on only the previous stratal unit, the autocorrelation function has a theoretical exponential form (Ndiaye, 2007a, 2007b). In contrast, in a purely periodic system, the autocorrelation will have multiple peaks separated by the wavelength of the signal (e.g. Drummond & Coates, 2000). For purely stochastic data, the function will never repeat, and will have an autocorrelation function consisting of a peak at the origin surrounded by low-level random background noise. As the recording of a periodic signal becomes increasingly inaccurate, the peaks broaden and become smaller with increasing lag. Autocorrelation results for the synthetic data set used for testing the spectral methods are shown in the Supporting Information.

Markov analyses have been applied to define the cyclicity of sedimentary successions (Carr, 1982; Harper, 1984a,

1984b; Miall, 1973; Powers & Easterling, 1982; Xu & MacCarthy, 1998). These analyses are based on the occurrence of a first-order Markov process and examine the probability of transitions between different facies in a stratigraphic succession. This study used the Harper (1984a, 1984b) method for Markov analysis, as implemented in Strati-Signal®. The binomial probability of each of the transitions was assessed at both the 85% and 70% levels of confidence. In general, the 85% level is used as the cut-off for transitions to be significant or weakly significant (Ndiaye, 2007a, 2007b) but it was necessary to use a more relaxed measure in order to examine the structure of weak cyclicity in the HD 14 section which shows only one statistically significant transition at the 85% confidence level.

Markov analysis should be preceded by a statistical test to determine whether the transitions are non-random. In this study, the randomness of the facies was assessed using the quasi-independence method (Goodman, 1968; Türk, 1979) in the Strati-Signal® software (Ndiaye, 2007a, 2007b).

7.2 | Autocorrelation results for facies data

The autocorrelation functions for the decompacted facies data for the HD 14, SHR and GH sections have a dominantly monotonic form, indicating an absence of consistent periodicity (Figure 9). At short lags (<1.5 to 2 m) the data can be fitted accurately by exponential decays. The exponential length scale of these decays is very small: 2.53 m for HD 14; 2.46 m for SHR; and 1.22 m for GH. These values are comparable to the average facies thickness after decompaction, e.g. the smaller value for GH reflects the smaller mean facies thickness for that section. This result suggests that the short-lag response is controlled largely by the uniformity of the response within each facies unit. This finding is supported by stratal-based autocorrelation and autoregression analyses (see Supporting Information) that indicated only minor statistical dependence of each facies unit on the preceding unit.

Autocorrelation functions for all three measured sections show significant departures from the exponential response at lags exceeding 2 m, indicating the occurrence of processes with longer-wavelength memory (Figure 9).

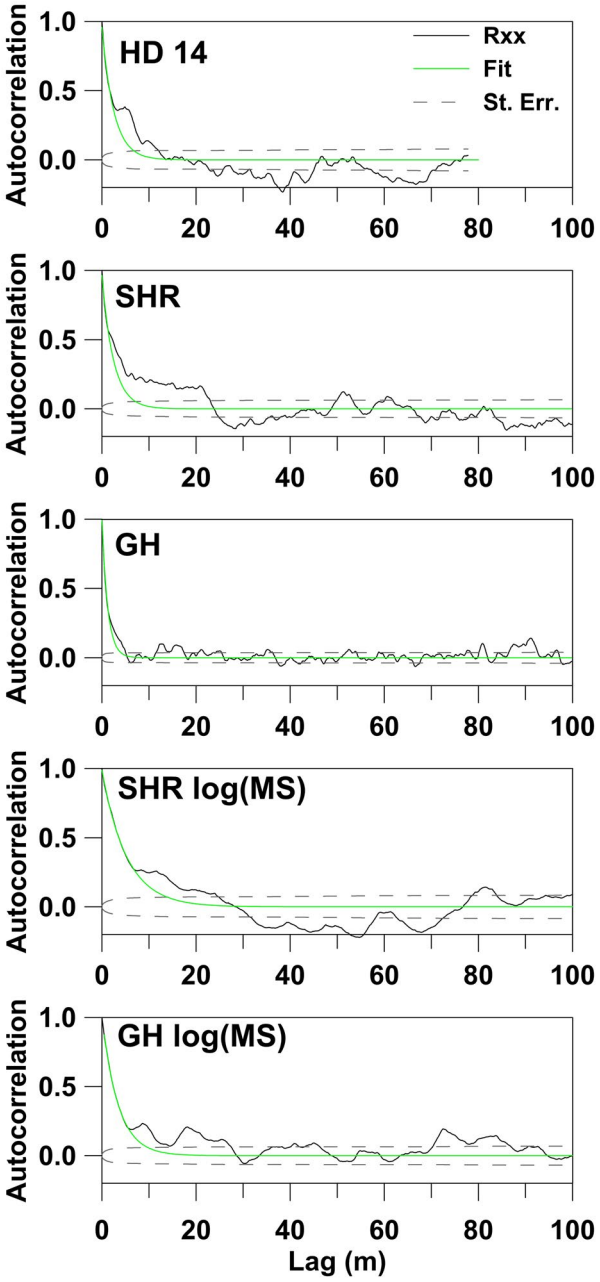

FIGURE 9 Autocorrelation response (Rxx) for decompacted facies and MS time series. The solid line shows the observed response, the dashed grey lines show the standard error level, and the green line shows the exponential function fitted to the lags of less than 1.5 to 2 m

1. For the HD 14 section, the autocorrelation function has a significant broad departure from the exponential model between 5 and 6 m and a weaker departure centred on 10 m. The 5–6 m departure can be related to the significant periodicity centred on this wavelength as seen in the wavelet and power spectra for the decompacted facies data (Figures 7 and 8). There is no evidence in the wavelet and power spectra for a peak at 10 m, suggesting that the 10 m autocorrelation response is most likely the second multiple of the 5–6 m peak.
2. For the SHR section, a strong departure in the observed autocorrelation response from an exponential function occurs over lags of 3–24 m, indicating processes with spatial coherence at these scales. This deviation is much more significant than in the other two sections. Although SHR decompacted facies spectra contain strong peaks at 10 m and 20 m wavelengths (Figures 7 and 11), the autocorrelation function contains no peaks at the corresponding lags. These results suggest that there is significant variation in the signal phase through the section.

3. For the GH section, the autocorrelation function is closer to an exponential response than the function for the other two sections. It includes small but statistically significant deviations from the exponential function centred on lags of 3–4 m, 12 m, and 17 m. The 3–4 m peak corresponds to the 3–4 m periodicity seen in the decompacted power spectra (Figure 8).
4. Autocorrelation results for all three sections also include long-lag features that can be related to the long-wavelength periodicity at the sections. The HD 14 response includes a positive peak between 45 and 55 m, the SHR response includes positive peaks between 50 and 60 m and between 70 and 80 m, and the GH response contains positive peaks between 80 and 90 m.

7.3 | Autocorrelation results for MS data

The autocorrelation functions for the MS data for the SHR and GH sections were calculated using decompacted and log-transformed data (Figure 9). The results exhibit significant non-random responses to lags of at least 27 m. The SHR MS autocorrelation resembles the facies result although it contains clearer increases centred on lags of about 12 and 22 m. These peaks coincide closely with spectral peaks at 10 m and 16–30 m in the power spectra of these data (Figure 8). The GH MS autocorrelation has peaks in similar positions to the SHR result but these peaks are defined more prominently against the background response.

As for the facies data, the MS autocorrelation data for the SHR and GH sections can be fitted accurately by exponential functions at short lags (<4 m). The SHR exponential function has a distance scale of 5.3 m (decompacted) and the GH function has a scale of 3.0 m (decompacted). These values are approximately twice the exponential scale values for the functions fitted to the corresponding facies data. The exponential scales for the MS data are independent of facies designations, and the results suggest there is a strong short-term memory in the data with a spatial scale of about twice the mean facies thickness.

7.4 | Crosscorrelation results

Crosscorrelation results were determined for the decompacted facies and MS data (Figure 10). Separate results were also computed for the lower and upper half of each section.

The crosscorrelation function for decompacted facies data for the whole HD 14 and SHR sections shows a significant positive correlation near zero lag (Figure 10). Correlation values reach a maximum of about 0.2 over a broad, irregularly shaped zone that includes the zero lag. This 0.2 value is statistically significant, but the relatively low value shows the data sets contain a high proportion of uncorrelated signals. The width of the peak is about 20 m which suggests that the component of the signal that is correlated has a scale length of around 10 to 20 m; that is, it is associated with relatively long-term variations rather than higher spatial frequency periodicity. Examination of the results for lower and upper halves of the HD 14 and SHR sections shows that the observed correlation is strong in the lower half and absent in the upper half. The correlation is attributed in large part to the siliciclastic rocks (facies G) in the lower 20 m of the SHR and HD 14 sections (Figure 2). The offset of the centre of the peak from zero lag can be explained by an approximate 10 m average offset between corresponding features on the two sections. Stratigraphic correlations suggest that an offset of around this size exists near the base of the section but larger offsets may occur higher in the section (Figure 2).

Crosscorrelation for decompacted facies data for the whole of the HD 14 and GH sections (Figure 10) shows no significant correlation but the corresponding results for the lower and upper half of each section show a weak positive correlation and strong negative correlation, respectively. The inconsistency of the results between the lower and upper halves of the sections suggests limited geological significance to the correlations. There is also no geologically significant correlation between the decompacted facies data for the SHR and GH sections (Figure 10).

Statistically significant correlation was observed between the decompacted facies and MS data for the SHR section (Figure 10). The observation of higher crosscorrelation in the lower half of the section and minimal crosscorrelation in the upper half indicates that the observed correlation is again due to the occurrence of facies G and higher susceptibility values in the lower 20 m of the section. In contrast, minimal crosscorrelation occurs between the observed facies and MS data for the GH section but there is a weak correlation for the lower half of the section.

The crosscorrelation for the MS data for the SHR and GH sections shows correlation at short wavelengths. The response includes statistically significant values in the 0.1–0.3 range between lags of −20 and +10 m. The observation of higher crosscorrelation in the lower half of the section and minimal crosscorrelation in the upper half indicates again that the observed correlation is associated with the higher MS values observed near the base of both sections.

7.5 | Markov analysis

The evaluation of quasi-independence (Goodman, 1968; Türk, 1979) of the HD 14, SHR and GH sections (Table 3) allows the rejection, at a 95% confidence level, of the

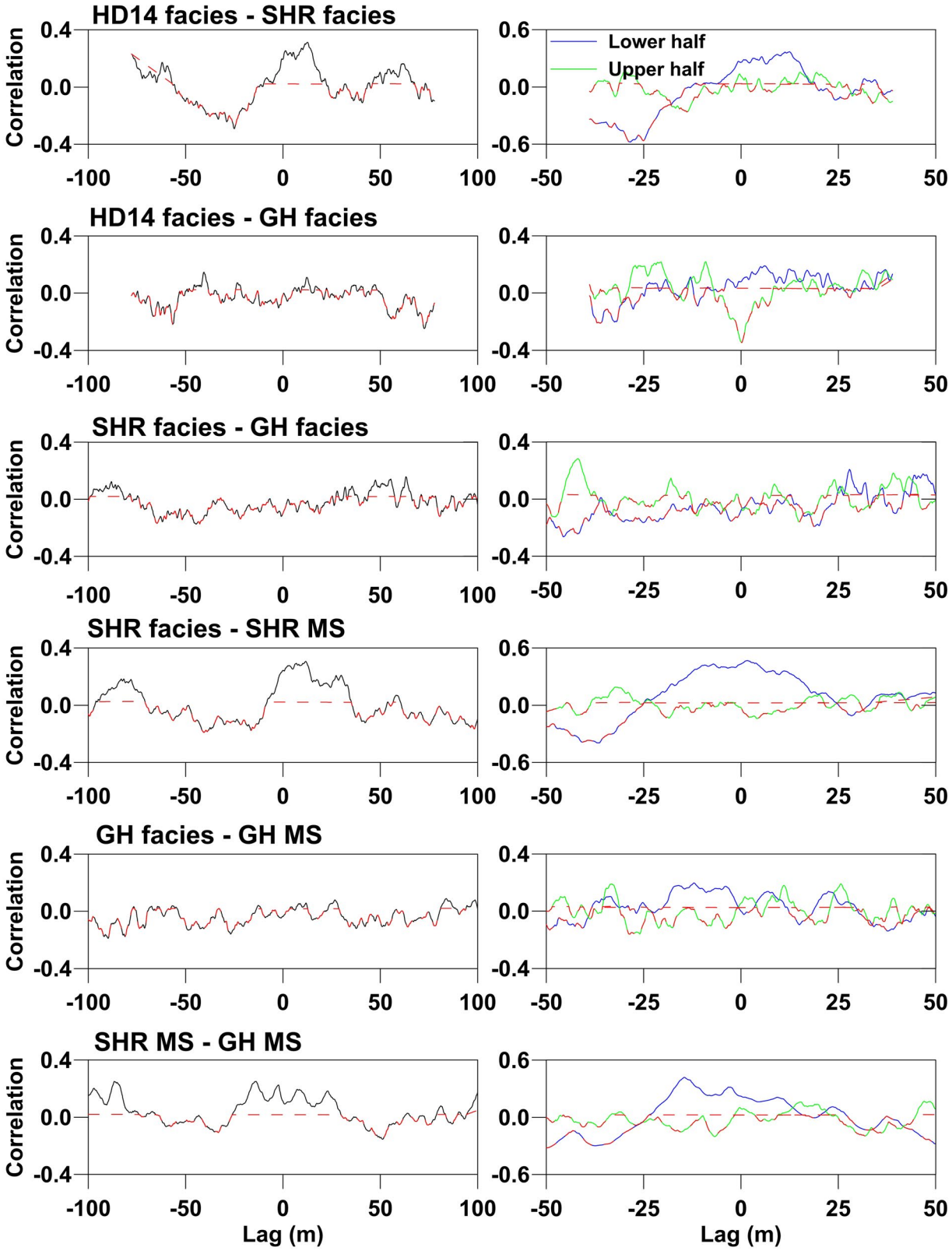

FIGURE 10 Crosscorrelation responses for decompacted facies and MS data. The solid line shows the observed response and the red dashed line show the f-test result for positive correlation. The left panels show the result for the whole section and the right panels show the results for the lower and upper half of each section. The upper three panels show the crosscorrelation of the facies data for the different measured sections. The fourth and fifth panels show the crosscorrelation of the decompacted facies response with the decompacted log-transformed MS data for the corresponding section. The lower panel shows the crosscorrelation of the decompacted log-transformed MS response for the SHR and GH sections

hypothesis that the upward transitions observed between facies in the Hull platform sections are random. The results suggest that the GH section has the fewest random transitions, with the highest ratio of observed χ^2 (chi-squared statistic) to theoretical χ^2 at 95% confidence (Table 3).

The more statistically significant transitions determined using the Markov analysis method of Harper (1984a, 1984b) are shown in Figure 11. Overall, the results include a greater number of statistically significant shallowing-upward facies transitions than deepening-upward transitions. In the SHR and GH sections, facies A (mudstones and associated coral–stromatoporoid–shelly limestones) is overlain by facies B (tabular stromatoporoid boundstones) or C (irregular–hemispherical stromatoporoid framestones) and then by facies D (stromatoporoid rudstones–floatstones). Facies D is followed by facies E (peloidal limestones) in the GH section and by facies A in the SHR section. Both sections also show an alternation between facies A and B. In the HD 14 section the statistical significance of the transitions is extremely low, and transitions only become significant at the 70% confidence level. The transition with the strongest significance is the transition from facies A to D. More weakly significant processes are a transition of facies C to D to F to C, as well as from facies C to E.

8 | ESTIMATION OF SEDIMENTATION RATE

Timescales can be assigned to the Hull platform signals using sedimentation rates. The rate estimated from the observed measured sections is here referred to as "compacted sedimentation rate", whereas the rate estimated from the sections after their correction for compaction is referred to as "decompacted sedimentation rate".

Sedimentation rates for the Hull platform sections are first estimated using the observed (compacted) thicknesses and interpreted durations of the sections. Based on the measured ~250 m thickness of the SHR and GH sections and their biostratigraphically constrained duration of 2.5 Myr ± 0.2–0.3 Myr the average compacted sedimentation rate for both sections is 0.1 m/kyr (Table 4). After the correction for compaction, the SHR and GH sections are 479 and 456 m thick, respectively, corresponding to decompacted sedimentation rates of 0.19 and 0.18 m/kyr.

The HD 14 section is shorter than the SHR and GH sections (7% shorter in the observed data); however, it is interpreted to represent a similar timescale. The section has a larger number of subaerial exposure surfaces than the SHR

TABLE 3 Results of χ^2 evaluation of facies transitions in the measured sections

Parameter	HD 14 section	SHR section	GH section
Number of transitions	92	144	179
Number of facies	7	7	6
Observed χ^2	65.8	54.4	70.2
Degrees of freedom	29	29	19
χ^2 at 95% confidence	42.6	42.6	30.1
Interpretation	Non-random	Non-random	Non-random

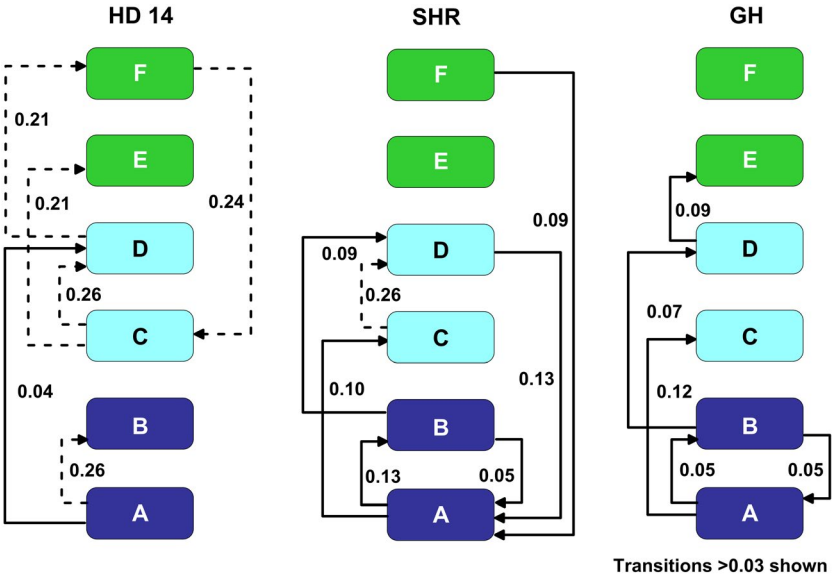

FIGURE 11 Statistically significant transitions between facies for the three measured sections determined using the Harper (1984a, 1984b) method. The numbers refer to the binomial probability for the transitions and only those transitions with a probability exceeding 0.03 are shown. Solid arrows with labels indicate transitions resolved at an 85% level of significance ($\alpha = 0.15$) and dashed arrows with labels indicate the additional transitions resolved at a 70% level of significance ($\alpha = 0.3$)

TABLE 4 Estimates of sedimentation rate

Parameter/section	HD 14	SHR	GH	HD 14	SHR	GH
	Observed/compacted			Decompacted		
Thickness/duration method						
Thickness (m)	238	257	256	—	479	456
Time (kyr)	2,500	2,500	2,500	2,500	2,500	2,500
Rate (m/kyr)	0.095	0.10	0.10	—	0.19	0.18
Visual spectral alignment for facies data						
Wavelength (m)	60	40	50	63	70	80
Period (kyr)	404	404	404	404	404	404
Rate (m/kyr)	0.15	0.10	0.12	0.16	0.17	0.20
ASM results for facies data						
C.L./H_0	99/25	99/56	99/0.51	95/4	95/5	95/77
Rate range (m/kyr)	0.14–0.15	0.08–0.10	0.10–0.12	0.20–0.22	0.16–0.18	0.19–0.21
TimeOpt results for facies + MS data						
Rate range (m/kyr)	0.13–0.14	0.10–0.12	0.11–0.12	0.20–0.23	0.20–0.22	0.23–0.25

Note: The decompaction correction was not applied to the uppermost 35 m of the HD 14 core so a decompacted sedimentation rate was not calculated for this section.

and GH sections, suggesting that loss due to exposure/erosion may be a significant factor.

The calculated sedimentation rates allow the estimation of the wavelength corresponding to the periods of Late Devonian Milankovitch signals (eccentricity cycles at 404, 124 and 95 kyr; obliquity cycles at 39 and 32 kyr; precession cycles at 20 and 17 kyr; Berger, Loutre, & Laskar, 1992). Both wavelet and power spectra show significant peaks near the expected Milankovitch periods (Figures 7 and 8). The position of the Milankovitch "comb" can be shifted relative to the spectral peaks, by adjusting the sedimentation rate, in order to improve the alignment of the peaks with the expected periods. Emphasis was placed on the optimal alignment of eccentricity cycles, the alignment was assessed visually, and the wavelength of the peak corresponding to the 404 kyr spectral line was used to calculate the sedimentation rate (Table 4). For the observed SHR and GH sections, this method yielded compacted sedimentation rates of 0.10 and 0.12 m/kyr, close to the rate of 0.1 m/kyr estimated using the section thickness and duration. The corresponding rates for the decompacted sections are 0.17 and 0.20 m/kyr. For the established sedimentation rates, the Nyquist wavelength corresponds to ~1 kyr for the facies data and ~20 kyr for the MS data. For the HD 14 section, it was difficult to align the Milankovitch comb with the spectrum. The method yielded a compacted sedimentation rate of 0.15 m/kyr but the result for the decompacted section of 0.16 m/kyr is inconsistent with this value.

The sedimentation rate was examined more rigorously using the Average Spectral Misfit (ASM) method (Meyers & Sageman, 2007), and the TimeOpt method (Meyers, 2015) (Table 4). The intent of these analyses was to confirm the presence of Milankovitch signals in the data rather than to establish the formal statistical significance of the results (e.g. as discussed in Da Silva et al., 2018; Da Silva et al., 2019; Hinnov, 2018; Hinnov, Wu, & Fang, 2016; Smith, 2019).

The ASM method evaluates the statistical significance of spectral peaks as a function of possible sedimentation rate (Meyers & Sageman, 2007). Sedimentation rates between 0.05 and 0.16 m/kyr were considered for the observed data, and rates between 0.10 and 0.25 m/kyr were considered for the decompacted data. ASM assesses the significance level of the null hypothesis (H_0) that the spectrum does not contain a periodic signal at one or more theoretical periods. The selection of periods for the observed sections was based on a 99% *F*-test significance level, whereas the analysis for the decompacted sections was based on a 95% significance level.

For the observed GH section and the decompacted SHR and HD 14 sections, the H_0 hypothesis can be rejected at a low significance level (between 0.5 and 5), indicating a good spectral fit (Figure 12a, Table 4). In contrast, the results for the observed SHR and HD 14 sections and the decompacted GH section exhibit only a broad minimum at a relatively high significance level. Despite the relatively high spectral misfit in these cases, there is good agreement between the results for the observed and decompacted data which, along with the very low significance level for some sections (e.g. the observed sections for GH and the decompacted section for SHR and HD 14), confirms the presence of Milankovitch signals in the facies data for the three sections and indicates compacted sedimentation rates between 0.08 and 0.15 m/kyr and decompacted sedimentation rates between 0.16 and 0.22 m/kyr.

The TimeOpt method determines the sedimentation rate that simultaneously optimises eccentricity amplitude modulation in the precession band, or longer-period eccentricity

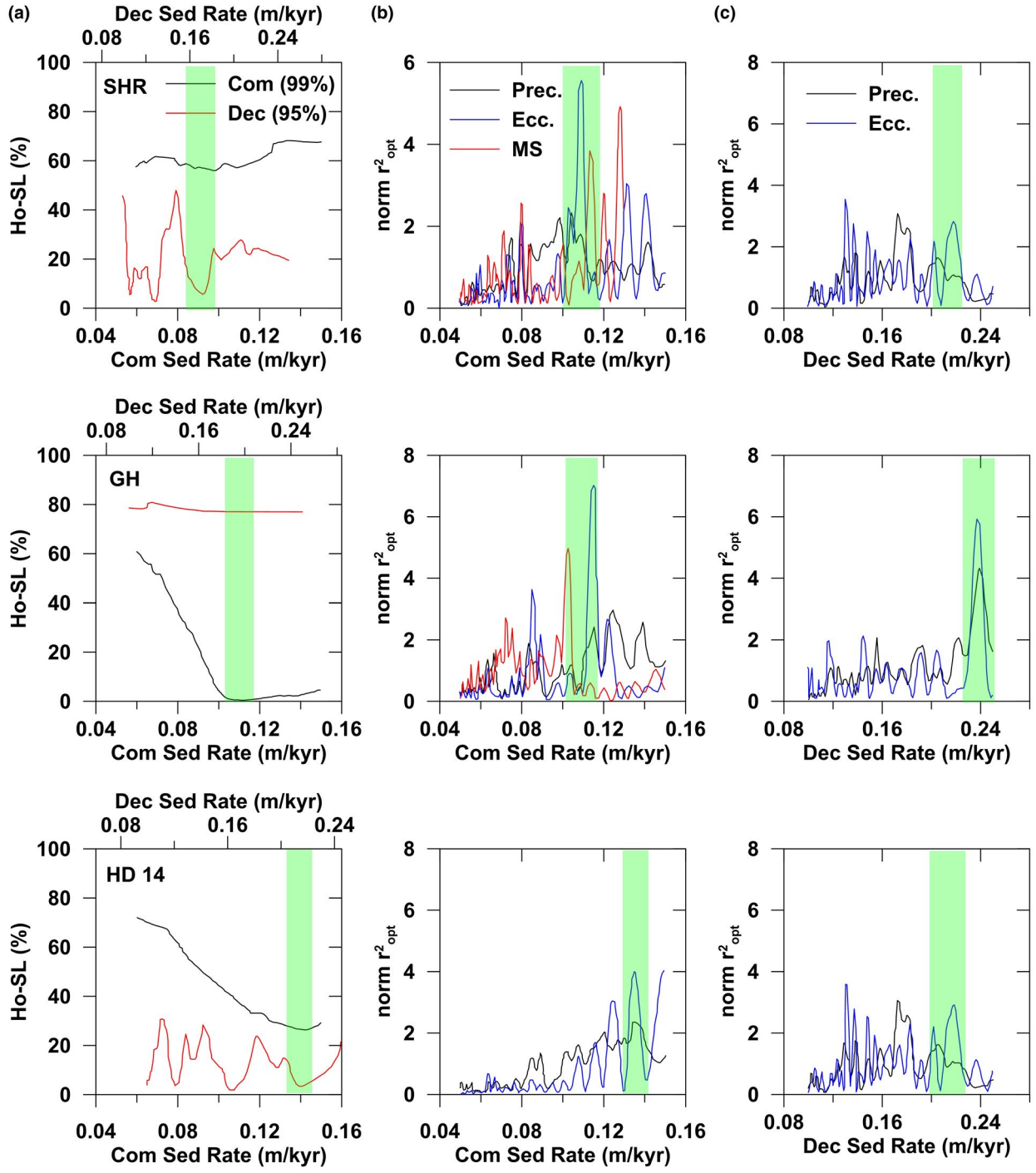

FIGURE 12 Average Spectral Misfit (ASM) and TimeOpt results. (a) ASM H_0 significance results for the observed section (99% *F*-test significance level) with compacted (Com) sedimentation rate shown on the lower axis and equivalent results for the decompacted section (95% *F*-test significance level) with decompacted (Dec) sedimentation rate shown on the upper axis. The two sedimentation rate axes are plotted with a differential scaling corresponding to the decompaction factor so that the optimal solution should be in approximately the same position for the observed and decompacted data. The green shading shows the range of optimal solutions chosen using both data sets. (b) TimeOpt results for the observed facies showing results for both the eccentricity amplitude modulations within the precession band (Prec.) and the long-period eccentricity amplitude modulations in the short-period eccentricity band (Ecc.) and results for MS showing the long-period eccentricity amplitude modulations in the short-period eccentricity band. The r^2_{opt} statistic for each analysis has been normalised to a unit mean value to allow plotting on the same vertical scale. The green shading shows the range of solutions defined by consideration of the various results. (c) TimeOpt results for the decompacted facies sections displayed using the same method as for the observed sections

amplitude modulation in the short period eccentricity band, and the concentration of power at precession and eccentricity periods (Meyers, 2015). The statistic examined is the product of the Pearson correlation coefficient for each of these parameters. In the present study, the results for both the precession and eccentricity modulations were normalised to a unit mean value to allow the direct comparison of the responses (Figure 12).

Comparison of ASM and TimeOpt results for the observed and decompacted facies and MS data and for the precession and eccentricity modulations (Figure 12) allows reliable identification of a small range of optimal sedimentation rates for each measured section (Table 4). For the observed SHR and GH sections, the visual, ASM and TimeOpt estimates of sedimentation rate are consistent at 0.10–0.12 m/kyr (Table 4). Values for decompacted SHR and GH sections show more variability, with TimeOpt results (0.21 and 0.24 m/kyr, respectively) being higher than those from the other two methods (0.17–0.18 and 0.19–0.21 m/kyr, respectively), or predicted from the observed section results and the decompaction factor. However, all these results indicate a decompacted sedimentation rate of ~0.2 m/kyr. For both SHR and GH sections, the thickness of the observed section is consistent with a 2.5 Myr sedimentation duration and the determined sedimentation rate, indicating that there has been minimal erosion in the SHR and GH sections.

For the observed HD 14 section, the visual, ASM and TimeOpt estimates of sedimentation rate are consistent at 0.14–0.15 m/kyr (Table 4). The ASM and TimeOpt results for the decompacted section are similar at 0.20–0.22 m/kyr which is consistent with the rate predicted using the observed section results and the decompaction factor. Comparison of the compacted sedimentation rate and 2.5 Myr duration for the HD 14 section with the measured 238 m thickness of the section indicates that about 35% of the observed section is absent.

Based on the calculated sedimentation rates, the longest term trends observed in the observed facies and MS data for the Hull platform sections (e.g. as seen in the observed cumulative facies-thickness deviation plots at spatial scales of 20 to 100 m; Figure 6) correspond to timescales of 200 kyr to 1 Myr. Spectral results for the measured sections indicate the longest wavelength periodic signal detected has a wavelength of 30–60 m in the observed data and 60–120 m in the decompacted data, indicating a period in the range 300–600 kyr. Spectral and autocorrelation results for the two sections indicate shorter wavelength periodic signals in the 2–12 m range in the observed data and 3–25 m in the decompacted data corresponding to periods in the range 20–120 kyr.

9 | EUSTATIC, TECTONIC AND AUTOGENIC SIGNATURES

Distinguishing between orbital forcing, local tectonic and autogenic responses in carbonate platforms is difficult because the processes all involve repeated, high-frequency changes in accommodation and operate on overlapping timescales (e.g. Bosence et al., 2009; De Benedictis et al., 2007; Kemp & Van Manen, 2019; Tucker & Garland, 2010; Westphal et al., 2010). Differentiation of these processes using numerical approaches requires careful consideration of the temporal and periodic form of the responses, but can be enhanced by information on spatial scales of the responses. The relative positions of the measured sections in this study (GH and SHR separated by ~1.5 km along-strike and located near the hangingwall of the fault block; GH and HD 14 separated by ~15.5 km; HD 14 located near the footwall margin) provide important spatial-scale information (Table 5).

Eustatic and climatic responses, which generally have large spatial scales, are identified in the Hull platform data as platform-wide responses with the same general form as the corresponding global signal. These responses must be observed at all measured sections in the study and, therefore, have a spatial scale of >16 km. Such responses include the occurrence of signals at eccentricity Milankovitch periods in wavelet and power spectral results for facies and MS data.

Strong evidence for local tectonic and/or autogenic controls on carbonate platform deposition is lateral discontinuity of small-scale sedimentary cycles (Bosence et al., 2009). Facies and MS results for the Hull platform exhibit this type of behaviour. Responses with significant differences between the three Hull platform sections include the facies-thickness distribution parameters and the timing and duration of periodic signals. Further differentiation between tectonic and autogenic processes can be done using the spatial scale and form of the responses. For example, signals that are present in two of the Hull platform sections, but absent from the third, suggest processes with spatial scales of 5 to 10 km and a tectonic origin. In contrast, local-scale responses with the expected statistical distribution of a random process suggest autogenic processes.

9.1 | Eustatic and climatic responses in the Hull platform

Possible eustatic responses in the Hull platform sections include signals associated with long timescale (>500 kyr) sea-level variations and shorter timescale (e.g. orbitally forced) variations. The presence of Milankovitch signals in the facies data provides a reliable indication of sea-level change. However, Milankovitch signals in MS data may be caused by both sea-level change and climatic variations (e.g. Crick et al., 1997; Da Silva et al., 2013).

Cumulative facies-thickness deviation plots for the Hull platform sections provide evidence of long-term (200 kyr to 1 Myr) non-periodic changes in facies distributions in the platform. Correlation of these plots with Fischer plots for

TABLE 5 Comparison of responses from the three measured sections for decompacted results

Parameter	HD 14 section	SHR section	GH section
Mean facies thickness (m)	1.92	2.55	1.83
Number of facies units in section	162	188	248
Dominant facies pair in thicker beds	E–F	A–B	A–B
Centre of largest long-wavelength peak in facies data (m)	45	65	80
Wavelength and wavelength range of additional large spectral peaks in facies data (m)	40 to >100 20–30 10–20 5–6	30 to >100 15–25 10 3–4	30 to >100 15–25 10–15 3–4
Length of segments of <30 m wavelength periodicity (m)	10	10–40	10–40
Wavelength range of large spectral peaks in MS response (m)	NA	40 to >100 12–30	40 to >100 20–30 8–10
Lags of positive peaks in autocorrelation of facies data (m)	4–6, 10 40–60	Broad, 3–24 50,60 70–85	3–4,12,16,24 80–95
Lags of positive peaks in autocorrelation of MS data (m)	NA	Broad 6–16 Broad 18–26	Peaked 8–12 Peaked 18–26
Markov cyclicity	Weak	Moderate	Moderate but higher than SHR
Facies involved in main cycles	C,D,E,F	A,B,C,D	A,B,C,D
Correlation of facies data with other sections	SHR (facies G effects)	HD 14 (facies G effects)	None
Correlation between facies and MS data at 10–20 m scale	NA	Moderate (facies G effects)	None

Abbreviation: NA, not applicable.

Frasnian successions from other continents, for example, western Canada, suggests the Canning Basin rocks record third-order eustatic variations (Brownlaw, 2000; Brownlaw et al., 1996).

Power spectra and wavelet results of facies and MS data for the SHR and GH sections have spectral peaks at, or close to, the eccentricity periods (Figures 7 and 8) providing significant evidence for the presence of Milankovitch periodicity and the recording of associated eustatic and climatic variations. For both measured sections, power level also increases at the expected period of the obliquity and precession periods but there are additional strong spectral lines between the eccentricity, obliquity, and precession periods that complicate the response. In contrast, power spectral results for the decompacted HD 14 section provide significantly weaker evidence for orbital forcing. ASM and TimeOpt analyses for the three Hull platform sections provide confirmation of Milankovitch signals and indicate decompacted sedimentation rates of about 0.2 m/kyr for all three sections.

The minimal correlation between facies and MS results for each Hull platform section, based on wavelet responses and crosscorrelation results, is attributed in part to the additional influence of climatic effects on detrital input and MS values (cf. Da Silva & Boulvain, 2006; Da Silva et al., 2013; Martinez, 2018; Whalen & Day, 2008).

Orbital periodicity in the Hull platform was investigated by Brownlaw, Hearn, and Jell (1998) and Brownlaw (2000) using Walsh transform power spectra for their Guppy Hills section. The authors used a spectral tuning approach to interpret spectral peaks in terms of Milankovitch periodicity. However, there is a degree of uncertainty in this interpretation because Walsh spectra may include spurious peaks at wavelengths longer than that of a true repeated signal (see Supporting Information). Nevertheless, the collective results of the previous and present studies suggest the presence of significant Milankovitch periodicity in the GH section.

Numerical evidence for eccentricity Milankovitch periods in the Hull platform sections (e.g. in terms of continuity of these signals in wavelet responses) is at a similar level to evidence from studies of Devonian successions in Europe and North America (De Vleeschouwer et al., 2014; Grabowski, Narkiewicz, & De Vleeschouwer, 2015; Pas et al., 2018). The poor resolution of the obliquity and precessional Milankovitch periods in the Hull platform facies and MS data is also similar to results from elsewhere (e.g. De Vleeschouwer et al., 2012; Ellwood, Algeo, El Hassani, Tomkin, & Rowe, 2011; Ellwood, Tomkin, et al., 2011). This poor resolution may be due in part to modulation of the signals by eccentricity responses (De Vleeschouwer et al., 2012; Hilgen et al., 2015; Kemp, 2011) with a potential contribution from short-term variability in sedimentation as discussed below. Stratigraphic distortions and fractally distributed hiatuses will have greatest effect on shorter period signals (Bailey & Smith, 2005; Hilgen et al., 2015; Martinez, Kotov, De Vleeschouwer, Damien, & Pälike, 2016).

9.2 | Tectonic and autogenic responses

Systematic differences in facies responses between the SHR and GH sections (located near the hangingwall margin) and those for the HD 14 section (located near the footwall margin) indicate that platform development on a tilted fault block resulted in consistent lateral facies variations, pointing to tectonic influence. Histogram and exceedence probability results for facies in each section (Figures 4 and 5, Table 5) indicate the thickest facies in the SHR and GH sections are dominantly moderate to deep-subtidal facies A and B, whereas the thickest facies in the HD 14 section are dominantly shallow-subtidal to intertidal facies E and F. Markov analysis indicates shallowing-upward cycles of facies A, B, C and D in the SHR and GH sections (Table 5). In contrast, the HD 14 section exhibits much weaker cyclicity but with the most consistent facies transitions occurring between facies C, D, E and F.

In the wavelet spectra, the patchiness of the Milankovitch eccentricity signal in all three measured sections (Figure 7, Table 5) indicates significant local-scale transient changes in the depositional response to Milankovitch driving that are interpreted to be due mainly to tectonic processes. The HD 14 section has the most strongly disrupted Milankovitch response of the three sections, consistent with its location closest to the footwall. Wavelet results for MS data reveal short-term variability in sedimentation rate and the occurrence of hiatuses that can be interpreted in terms of tectonic forcing. For example, in the SHR section, the long period responses at heights above 200 m in the observed section (above 375 m in the decompacted section) exhibit a drift with time to shorter periods, consistent with a short-term decrease in the sedimentation rate (Figures 7 and 12). The GH section exhibits an abrupt change in the 40 m wavelength peak at 70 m height in the observed section that is manifest as a bifurcation in the wavelet spectral response (Figure 7) and can be explained by a depositional hiatus (cf. Meyers, Sageman, & Hinnov, 2001). This response corresponds with the subaerial unconformity in the Hull platform succession (Figure 2) which is interpreted to have been controlled in large part by footwall uplift (George, Chow, et al., 2009).

Other evidence of tectonic influence is provided by the cumulative facies-thickness deviation curves, which show differences in the pattern of the 20 to 50 m spaced peaks for the SHR and GH sections (decompacted data) but even larger differences for the HD 14 section (Figure 6).

Facies and MS data for the Hull platform have a strong stochastic component, providing strong evidence for autogenic controls (cf. Burgess, 2006; Wilkinson et al., 1999). The stochastic response is particularly evident at spatial scales of less than 2–3 m in the observed data (<5–6 m in the decompacted data). Exceedence probability results for facies thickness follow an exponential distribution over this spatial scale. The results exhibit a change in fractal scale between about 2 and 4 m (Figure 5), suggesting strong control from orbital driving and tectonic processes at longer wavelengths. Further evidence for the stochastic response comes from the autocorrelation, autoregression and Markov analyses (Figures 9 and 11, Table S1 in Supporting Information) which indicate minimal dependence between a facies unit and the underlying facies units.

Perhaps the strongest evidence for an autogenic response for the Hull platform is the lateral discontinuity between the closely spaced SHR and GH sections (Figures 1 and 2; cf. Eberli, 2013; Samankassou & Enos, 2019). Although the criterion of lateral continuity must be applied carefully (e.g. Westphal et al., 2010), significant differences between the

two sections are evident. Mean facies thickness is 20% less in the GH section than in the SHR section. Facies autocorrelation responses, at lags of less than 20 m, show the GH function has clear narrow peaks, whereas the SHR function has a broad peak (Figure 9). Spectral peaks in each measured section occur at slightly different wavelengths and there is variation in the timing, duration, and exact frequency of the signal in the zones of enhanced periodicity in each section.

10 | CONCLUSIONS AND IMPLICATIONS

The present study applied multi-method numerical analyses to facies and MS data to show that Hull platform sedimentation was controlled by a complex interplay of global orbital forcing and local tectonic and autogenic processes. These results have significant implications both for improved understanding of the controls on Frasnian reef development in the Canning Basin and for highlighting the value of using a full suite of numerical analysis methods, including time-based, frequency-based and spatially based methods, on complicated data sets from ancient shallow-water carbonate successions in tectonically active settings.

Evidence for Milankovitch cyclicity in all three Hull platform sections is provided by wavelet spectra and power spectra showing peaks corresponding to the 404, 124 and 95 kyr orbital eccentricity responses, and general increases in signal level at the expected position of orbital obliquity and precession periods. ASM and TimeOpt methods provide confirmation of the presence of Milankovitch cyclicity in both the facies and MS data. Significant spatial and temporal differences along the Hull platform (hangingwall SHR and GH sections versus footwall HD 14 section), as indicated by histogram and exceedence probability results for facies thickness, Markov analysis and wavelet spectral results, as well as the variability and interruptions in the Milankovitch record, confirm the important role of tectonic forcing due to syndepositional fault-block rotation. The high stochastic element in the probability exceedence, spectral, correlation, autoregression and Markov responses of the closely spaced SHR and GH sections indicates significant variation in facies distribution between the sections that is consistent with autogenic processes.

Studies of other Frasnian platforms in the Canning Basin have described metre-scale and larger scale sedimentary cycles, based on lithofacies observations and discussed the potential role of orbital forcing and tectonic activity (e.g. Hocking & Playford, 2000; Playford et al., 2009; Playford et al., 1989; Read, 1973). Statistical analyses were not done because of concerns about variable deposition rates and compaction effects between different facies and, therefore, the use of lithofacies thickness as indicators of time (Playford et al., 2009). Recent sequence stratigraphic and isotope chemostratigraphic studies of Frasnian foreslope successions in the Canning Basin have postulated that sequence architecture was controlled mainly by global eustatic processes based on comparison with coeval data sets in North America and Europe (Hillbun et al., 2016; Playton et al., 2016; Playton & Kerans, 2015). Although local tectonic activity was considered a potential driver, no further work was done in these studies to try distinguishing the responses of the different mechanisms. Application of the numerical approach used in the present study to other Frasnian platforms and to Frasnian foreslopes of the Canning Basin, where detailed data sets are available, may help us to distinguish the different eustatic, climatic, tectonic and autogenic signals preserved in these successions and to improve our understanding of the evolution of Devonian reef complexes in the Canning Basin.

The signal of Milankovitch cycles in the geologic record has been used extensively as a basis for refining geological timescales (e.g. Hinnov, 2018; Strasser, 2018). However, major challenges have been identified in using a cyclostratigraphic and astrochronologic approach that are related in part to potential overprint or contamination of orbital signals by stochastic climate variability, autogenic variability and diagenesis, and to stratigraphic distortions caused by variable sedimentation and compaction rates and hiatuses (Meyers, 2019). The present study demonstrates that a multi-method numerical approach is needed in order to verify Milankovitch signals in an ancient carbonate platform, such as the Hull platform, where syndepositional tectonic activity and autogenic processes have complicated the stratigraphic record. Initial numerical analysis using only power spectral analysis provided a confusing response with an equivocal suggestion of Milankovitch periodicity in a dominantly stochastic response. Application of a broader suite of numerical analysis methods, including time-frequency spectral analyses, geostatistical analyses and correlation and Markov analyses, provided increased resolution and understanding of the multiple processes involved.

Overlapping temporal and spatial scales of orbitally forced, tectonically forced and autogenic cyclicity in carbonate platform rocks means that it is commonly difficult to discriminate between these sources. This study shows that a solid understanding of the facies architecture of a carbonate platform succession, based on field and drillcore observations, is key background knowledge for numerical-based studies. The three Hull platform sections were selected for this study because they represent footwall and hangingwall positions on an active fault block. This approach better enabled recognition of local responses due to variable sedimentation rates and hiatuses caused by accommodation changes related to fault-block tilting and to autogenic variability in the Hull platform.

Although it was not a core objective of this study, the results from the three Hull platform sections emphasise the uncertainty that can arise in estimating sedimentation rates from shallow-water carbonate successions (e.g. Eberli, 2013; Samankassou & Enos, 2019; Weij, Reijmer, Eberli, & Swart, 2018). For example, sedimentation rates based on the HD 14 section alone would be significantly underestimated because of the amount of missing section due to subaerial exposure/erosion. Likewise, the temporal variability in the wavelet spectra for all three measured sections shows that sedimentation rates determined from short time segments would be poor estimates of the long-term rate. Sufficient spatial and temporal sampling of the platform succession is needed to maximise the accuracy of quantitative estimates such as sedimentation or accumulation rate.

ACKNOWLEDGEMENTS

Much of this study was completed during research leave visits in 2008, 2014, and 2019 to the University of Western Australia by IJF and NC, the first of which involved valuable support from UWA Gledden Senior Visiting Fellowships. IJF is supported by Natural Sciences and Engineering Research Council of Canada Discovery Grant RGPIN-005475-2017, and ACDS is supported by Fonds de la Recherche Scientifique Grant FNRS-PDR-T.0051.19. We acknowledge IGCP-652 (UNESCO) Project: Reading Geologic Time in Paleozoic Sedimentary Rocks. We thank Peter Isaacson, Peter Burgess and two anonymous reviewers for helpful comments that improved the manuscript.

CONFLICT OF INTEREST

The authors have no conflict of interest to declare.

DATA AVAILABILITY STATEMENT

Data Availability Statement: The data that support the findings of this study are openly available from the University of Western Australia (UWA) Research Repository at https://doi.org/10.26182/5eb901d06c136

ORCID

Ian J. Ferguson https://orcid.org/0000-0001-5074-5666
Anne-Christine Da Silva https://orcid.org/0000-0003-4191-7600
Nancy Chow https://orcid.org/0000-0002-3092-519X
Annette D. George https://orcid.org/0000-0002-9987-6592

REFERENCES

AGICO. (2003). *Kappabridge KLY-3/KLY-3S user's manual (Ver. 2.3)*. Retrieved from https://www.agico.com/downloads/documents/manuals/kly3-man.pdf

Bailey, R. J., & Smith, D. G. (2005). Quantitative evidence for the fractal nature of the stratigraphic record: Results and implications. *Proceedings of the Geological Association*, *116*, 129–138. https://doi.org/10.1016/S0016-7878(05)80004-5

Becker, R. T., Gradstein, F. M., & Hammer, O. (2012). The Devonian Period. In: F. M. Gradstein, J. G. Ogg, M. D. Schmitz, & G. M. Ogg (Eds.), *The geologic time scale 2012* (pp. 559–601). Amsterdam: Elsevier.

Belkhedim, S., Jarochowska, E., Benhamou, M., Nemra, A., Sadji, R., & Munnecke, A. (2019). Interplay of autogenic and allogenic processes on the formation of shallow carbonate cycles in a synrift setting (Lower Pliensbachian, Traras Mountains, NW Algeria). *Journal of Sedimentary Research*, *89*, 784–807. https://doi.org/10.2110/jsr.2019.33

Berger, A., Loutre, M. F., & Laskar, J. (1992). Stability of the astronomical frequencies over the Earth's history for paleoclimate studies. *Science*, *255*, 560–566. https://doi.org/10.1126/science.255.5044.560

Bosence, D., Procter, E., Aurell, M., Kahla, A. B., Boudagher-Fadel, M., Casaglia, F., … Waltham, D. (2009). A dominant tectonic signal in high-frequency, peritidal carbonate cycles? A regional analysis of Liassic platforms from Western Tethys. *Journal of Sedimentary Research*, *79*, 389–415. https://doi.org/10.2110/jsr.2009.038

Boulila, S., Galbrun, B., Huret, E., Hinnov, L. A., Rouget, I., Gardin, S., & Bartolini, A. (2014). Astronomical calibration of the Toarcian Stage: Implications for sequence stratigraphy and duration of the early Toarcian OAE. *Earth and Planetary Science Letters*, *386*, 98–111. https://doi.org/10.1016/j.epsl.2013.10.047

Brownlaw, R. L. S. (2000). Rugose coral stratigraphy and cyclostratigraphy of the Middle and Upper Devonian carbonate complexes, Lennard Shelf, Canning Basin, Western Australia. Ph.D. Thesis, University of Queensland, Brisbane, Australia, 325 p.

Brownlaw, R. L. S., Hearn, S. J., & Jell, J. S. (1998). Spectral analysis of the back-reef limestones of the "Devonian Great Barrier Reef", Western Australia. *Proceedings of the Royal Society of Queensland*, *107*, 99–107.

Brownlaw, R. L. S., Hocking, R. M., & Jell, J. S. (1996). High frequency sea-level fluctuations in the Pillara Limestone, Guppy Hills, Lennard Shelf, Northwestern Australia. *Historical Biology*, *11*, 187–212. https://doi.org/10.1080/10292389609380541

Brownlaw, R. L. S., & Jell, J. S. (2008). Middle and Upper Devonian rugose corals from the Canning Basin, Western Australia. *Memoirs of the Association of Australasian Palaeontologists*, *35*, 1–126.

Burgess, P. M. (2006). The signal and the noise: Forward modeling of allocyclic and autocyclic processes influencing peritidal carbonate stacking patterns. *Journal of Sedimentary Research*, *76*, 962–977. https://doi.org/10.2110/jsr.2006.084

Burgess, P. M. (2016). Identifying ordered strata: Evidence, methods, and meaning. *Journal of Sedimentary Research*, *86*, 148–167. https://doi.org/10.2110/jsr.2016.10

Burgess, P. M., Wright, V. P., & Emery, D. (2001). Numerical forward modelling of peritidal carbonate parasequence development: Implications for outcrop interpretation. *Basin Research*, *13*, 1–16. https://doi.org/10.1046/j.1365-2117.2001.00130.x

Carr, T. R. (1982). Log-linear models, Markov chains and cyclic sedimentation. *Journal of Sedimentary Petrology*, *52*, 905–912. https://doi.org/10.1306/212F808A-2B24-11D7-8648000102C1865D

Chen, C., & Hiscott, R. N. (1999a). Statistical analysis of turbidite cycles in submarine fan successions: Tests for short-term persistence. *Journal of Sedimentary Research*, *69*, 486–504. https://doi.org/10.2110/jsr.69.486

Chen, C., & Hiscott, R. N. (1999b). Statistical analysis of facies clustering in submarine-fan turbidite successions. *Journal of Sedimentary Research*, *69*, 505–517. https://doi.org/10.2110/jsr.69.505

Chen, D., Tucker, M. E., Jiang, M., & Zhu, J. (2001). Long-distance correlation between tectonic controlled, isolated carbonate platforms by cyclostratigraphy and sequence stratigraphy in the Devonian of South China. *Sedimentology*, *48*, 57–78. https://doi.org/10.1111/j.1365-3091.2001.00351.x

Chow, N., George, A. D., & Trinajstic, K. M. (2004). Tectonic control on development of a Frasnian-Famennian (Late Devonian) palaeokarst surface, Canning Basin reef complexes, northwestern Australia. *Australian Journal of Earth Sciences*, *51*, 911–917. https://doi.org/10.1111/j.1400-0952.2004.01493.x

Chow, N., George, A. D., Trinajstic, K. M., & Chen, Z. Q. (2013). Stratal architecture and platform evolution of an early Frasnian syn-tectonic carbonate platform, Canning Basin, Australia. *Sedimentology*, *60*, 1583–1620. https://doi.org/10.1111/sed.12041

Crick, R. E., Ellwood, B. B., Hladil, J., El Hassani, A., Feist, R., & Hladil, J. (1997). Magnetosusceptibility event and cyclostratigraphy (MSEC) of the Eifelian -Givetian GSSP and associated boundary sequences in North Africa and Europe. *Episodes*, *20*, 167–175. https://doi.org/10.18814/epiiugs/1997/v20i3/004

Da Silva, A. C., & Boulvain, F. (2006). Upper Devonian carbonate platform correlations and sea level variations recorded in magnetic susceptibility. *Palaeogeography, Palaeoclimatology, Palaeoecology*, *240*, 373–388. https://doi.org/10.1016/j.palaeo.2006.02.012

Da Silva, A. C., De Vleeschouwer, D., Boulvain, F., Claeys, P., Fagel, N., Humblet, M., … Dekkers, M. J. (2013). Magnetic susceptibility as a high-resolution correlation tool and as a climatic proxy in Paleozoic rocks – Merits and pitfalls: Examples from the Devonian in Belgium. *Marine and Petroleum Geology*, *46*, 173–189. https://doi.org/10.1016/j.marpetgeo.2013.06.012

Da Silva, A. C., Dekkers, M. J., De Vleeschouwer, D., Hladil, J., Chadimova, L., Slavík, L., & Hilgen, F. J. (2018). Millennial-scale climate changes manifest Milankovitch combination tones and Hallstatt solar cycles in the Devonian greenhouse world. *Geology*, *47*, 19–22. https://doi.org/10.1130/G45511.1

Da Silva, A. C., Dekkers, M. J., De Vleeschouwer, D., Hladil, J., Chadimova, L., Slavík, L., & Hilgen, F. J. (2019). Millennial-scale climate changes manifest Milankovitch combination tones and Hallstatt solar cycles in the Devonian greenhouse world: REPLY. *Geology*, *47*, e489–e490. https://doi.org/10.1130/G46732Y.1

Da Silva, A. C., Hladil, J., Chadimova, L., Slavík, L., Hilgen, F. J., Bábek, O., & Dekkers, M. J. (2016). Refining the Early Devonian time scale using Milankovitch cyclicity in Lochkovian-Pragian sediments (Prague Synform, Czech Republic). *Earth and Planetary Science Letters*, *455*, 125–139. https://doi.org/10.1016/j.epsl.2016.09.009

Da Silva, A. C., Mabille, C., & Boulvain, F. (2009). Influence of sedimentary setting on the use of magnetic susceptibility: Examples from the Devonian of Belgium. *Sedimentology*, *56*, 1292–1306. https://doi.org/10.1111/j.1365-3091.2008.01034.x

Da Silva, A. C., Potma, K., Weissenberger, J. A. W., Whalen, M. T., Mabille, C., & Boulvain, F. (2009). Magnetic susceptibility evolution and sedimentary environments on carbonate platform sediments and atolls, comparison of the Frasnian from Belgium and from Alberta. *Sedimentary Geology*, *214*, 3–18. https://doi.org/10.1016/j.sedgeo.2008.01.010

Da Silva, A. C., Whalen, M. T., Hladil, J., Chadimova, L., Chen, D., Spassov, S., … Devleeschouwer, X. (2015). Magnetic susceptibility application: a window onto ancient environments and climatic variations: foreword. In: A. C. Da Silva, & M. T. Whalen J. Hladil, L. Chadimova, D. Chen, S. Spassov, F. Boulvain, & X. Devleeschouwer (Eds.), *Magnetic susceptibility application: a window onto ancient environments and climate* (Vol. *414*, pp. 1–13). Geological Society, London, Special Publications. https://doi.org/10.1144/SP414.12

De Benedictis, D., Bosence, D., & Waltham, D. (2007). Tectonic control on peritidal carbonate parasequence formation: An investigation using forward tectono-stratigraphic modelling. *Sedimentology*, *54*, 587–605. https://doi.org/10.1111/j.1365-3091.2006.00851.x

De Vleeschouwer, D., Boulvain, F., Da Silva, A. C., Pas, D., Labaye, C., & Claeys, P. (2014). The astronomical calibration of the Givetian (Middle Devonian) timescale (Dinant Synclinorium, Belgium). In: A. C. Da Silva, M. T. Whalen, J. Hladil, L. Chadimova, D. Chen, S. Spassov, F. Boulvain, & X. Devleeschouwer (Eds.), *Magnetic susceptibility application: a window onto ancient environments and climate* (Vol. *414*, pp. 245–256). Geological Society, London, Special Publications. https://doi.org/10.1144/SP414.3

De Vleeschouwer, D., Da Silva, A. C., Sinnesael, M., Chen, D., Day, J. E., Whalen, M. T., … Claeys, P. (2017). Timing and pacing of the Late Devonian mass extinction event regulated by eccentricity and obliquity. *Nature Communications*, *8*, 2268. https://doi.org/10.1038/s41467-017-02407-1

De Vleeschouwer, D., Rakociński, M., Racki, G., Bond, D. P., Sobień, K., & Claeys, P. (2013). The astronomical rhythm of Late-Devonian climate change (Kowala section, Holy Cross Mountains, Poland). *Earth and Planetary Science Letters*, *365*, 25–37. https://doi.org/10.1016/j.epsl.2013.01.016

De Vleeschouwer, D., Whalen, M. T., Day, J. E., & Claeys, P. (2012). Cyclostratigraphic calibration of the Frasnian (Late Devonian) time-scale (Western Alberta, Canada). *GSA Bulletin*, *124*, 928–942. https://doi.org/10.1130/B30547.1

Doglioni, C., & Goldhammer, R. K. (1988). Compaction-induced subsidence in the margin of a carbonate platform. *Basin Research*, *1*, 237–246. https://doi.org/10.1111/j.1365-2117.1988.tb00019.x

Dörling, S. L., Dentith, M. C., Groves, D. I., Playford, P. E., Vearncombe, J. R., Muhling, P., & Windrim, D. (1996). Heterogeneous brittle deformation in the Devonian carbonate rocks of the Pillara Range, Canning Basin: Implications for the structural evolution of the Lennard Shelf. *Australian Journal of Earth Sciences*, *43*, 15–29. https://doi.org/10.1080/08120099608728232

Dorobek, S. L. (2008). Tectonic and depositional controls on syn-rift carbonate platform sedimentation. In: J. Lukasik, & J. A. Simo (Eds.), *Controls on carbonate platform and reef development* (Vol. 89, pp. 57–81). Society of Sedimentary Geology, Special Publication. https://doi.org/10.2110/pec.08.89.0057

Drummond, C. N. (1999). Bed-thickness structure of multi-sourced ramp turbidites: Devonian Brallier Formation, Central Appalachian Basin. *Journal of Sedimentary Research*, *69*, 115–121. https://doi.org/10.2110/jsr.69.115

Drummond, C. N., & Coates, J. (2000). Exploring the statistics of sedimentary bed thicknesses - two case studies. *Journal of Geoscience Education*, *48*, 487–499. https://doi.org/10.5408/1089-9995-48.4.487

Eberli, G. P. (2013). The uncertainties involved in extracting amplitude and frequency of orbitally driven sea-level fluctuations from shallow-water carbonate cycles. *Sedimentology*, *60*, 64–84. https://doi.org/10.1111/sed.12011

Ellwood, B. B., Algeo, T. J., El Hassani, A., Tomkin, J. H., & Rowe, H. D. (2011). Defining the timing and duration of the Kačák Interval within the Eifelian/Givetian boundary GSSP, Mech Irdane,

Morocco, using geochemical and magnetic susceptibility patterns. *Palaeogeography, Palaeoclimatology, Palaeoecology*, *304*, 74–84. https://doi.org/10.1016/j.palaeo.2010.10.012

Ellwood, B. B., Crick, R. E., El Hassani, A., Benoist, S. L., & Young, R. H. (2000). Magnetosusceptibility event and cyclostratigraphy method applied to marine rocks: Detrital input versus carbonate productivity. *Geology*, *28*, 1135–1138. https://doi.org/10.1130/0091-7613(2000)28%3C1135:MEACMA%3E2.0.CO;2

Ellwood, B. B., Tomkin, J. H., El Hassani, A., Bultynck, P., Brett, C. E., Schindler, E., … Bartholomew, A. J. (2011). A climate-driven model and development of a floating point time scale for the entire Middle Devonian Givetian Stage: A test using magnetostratigraphy susceptibility as a climate proxy. *Palaeogeography, Palaeoclimatology, Palaeoecology*, *304*, 85–95. https://doi.org/10.1016/j.palaeo.2010.10.014

Ellwood, B. B., Wang, W. H., Tomkin, J. H., Ratcliffe, K. T., El Hassani, A., & Wright, A. M. (2013). Testing high resolution magnetic susceptibility and gamma radiation methods in the Cenomanian-Turonian (Upper Cretaceous) GSSP and near-by coeval section. *Palaeogeography, Palaeoclimatology, Palaeoecology*, *378*, 75–90. https://doi.org/10.1016/j.palaeo.2013.02.018

Fischer, A. G. (1964). The Lofer cyclothems of the Alpine Triassic. In: D. F. Merriam (Ed.), *Symposium on cyclic sedimentation* (Vol. *169*, pp. 107–149). Kansas Geological Survey Bulletin.

García-Alcalde, J. L., Ellwood, B. B., Soto, F., Truyóls-Massoni, M., & Tomkin, J. H. (2012). Precise timing of the Upper Taghanic Biocrisis, Geneseo Bioevent, in the Middle-Upper Givetian (Middle Devonian) boundary in Northern Spain using biostratigraphic and magnetic susceptibility data sets. *Palaeogeography, Palaeoclimatology, Palaeoecology*, *313–314*, 26–40. https://doi.org/10.1016/j.palaeo.2011.10.006

George, A. D., Chow, N., & Trinajstic, K. M. (2009). Syndepositional fault control on Lower Frasnian platform evolution, Lennard Shelf, Canning Basin, Australia. *Geology*, *37*, 331–334. https://doi.org/10.1130/G25461A.1

George, A. D., Trinajstic, K. M., & Chow, N. (2009). Frasnian reef evolution and palaeogeography, SE Lennard Shelf, Canning Basin, Australia. In: P. Könighsof (Ed.), *Devonian change: case studies in palaeogeography and palaeoecology* (Vol. *314*, pp. 73–107). Geological Society, London, Special Publications. doi: 10.1144/SP314.4. https://doi.org/10.1144/SP314.4

Goldhammer, R. K. (1997). Compaction and decompaction algorithms for sedimentary carbonates. *Journal of Sedimentary Research*, *67*, 26–35. https://doi.org/10.1306/D42684E1-2B26-11D7-8648000102C1865D

Goldhammer, R. K., Lehmann, P. J., & Dunn, P. A. (1993). The origin of high-frequency platform carbonate cycles and third-order sequences (Lower Ordovician El Paso Gp, West Texas); constraints from outcrop data and stratigraphic modeling. *Journal of Sedimentary Research*, *63*, 318–359. https://doi.org/10.1306/D4267AFA-2B26-11D7-8648000102C1865D

Goodman, L. A. (1968). The analysis of cross-classified data: Independence, quasi-independance and interactions in contingency tables with or without missing entries. *Journal of the American Statistical Association*, *63*, 1091–1131. https://doi.org/10.1080/01621459.1968.10480916

Grabowski, J., Narkiewicz, M., & De Vleeschouwer, D. (2015). Forcing factors of the magnetic susceptibility signal in lagoonal and subtidal depositional cycles from the Zachełmie section (Eifelian, Holy Cross Mountains, Poland). In: A. C. Da Silva, M. T. Whalen, J. Hladil, L. Chadimova, D. Chen, S. Spassov, F. Boulvain, & X. Devleeschouwer (Eds.), *Magnetic susceptibility application: A window onto ancient environments and climate* (Vol. *414*, pp. 225–244). Geological Society, London, Special Publications. https://doi.org/10.1144/SP414.5

Harper, C. W. J. (1984a). Facies model revisited: An examination of quantitative methods. *Geoscience Canada*, *11*, 203–207.

Harper, C. W. J. (1984b). Improved methods of facies sequence analysis, In: R. G. Walker (Ed.), *Facies models* (Second Edition, pp. 1–13), Geoscience Canada Reprint Series 1, Geological Association of Canada.

Hilgen, F. J., Hinnov, L. A., Aziz, H. A., Abels, H. A., Batenburg, S., Bosmans, J. H., … Zeeden, C. (2015). Stratigraphic continuity and fragmentary sedimentation: the success of cyclostratigraphy as part of integrated stratigraphy. In: D. G. Smith, R. J. Bailey, P. M. Burgess, & A. J. Fraser (Eds.), *Strata and time: Probing the gaps in our understanding* (Vol. *404*, pp. 157–197). Geological Society, London, Special Publications. https://doi.org/10.1144/SP404.12

Hill, J., Wood, R., Curtis, A., & Tetzlaff, D. M. (2012). Preservation of forcing signals in shallow water carbonate sediments. *Sedimentary Geology*, *275*, 79–92. https://doi.org/10.1016/j.sedgeo.2012.07.017

Hillbun, K. N. (2015). Re-evaluating the late devonian mass extinction: A geochemical investigation of the relationship between carbon isotope fluctuations, faunal turnover, and paleoenvironmental change recorded in Upper Devonian carbonates of the Lennard Shelf, Western Australia. Ph.D. Thesis, Seattle: University of Washington, 266 p.

Hillbun, K., Playton, T. E., Katz, D. A., Tohver, E., Trinajstic, K., Haines, P. W., … Montgomery, P. (2016). Correlation and sequence stratigraphic interpretation of Upper Devonian carbonate slope facies using carbon isotope chemostratigraphy, Lennard Shelf, Canning Basin, Western Australia. In: T. E. Playton, C. Kerans, & J. A. W. Weissenberger (Eds.), *New advances in Devonian carbonates: outcrop analogs, reservoirs, and chronostratigraphy* (Vol. *107*, pp. 248–301). SEPM Special Publication. https://doi.org/10.2110/sepmsp.107.09

Hinnov, L. A. (2000). New perspectives on orbitally forced stratigraphy. *Annual Review of Earth and Planetary Sciences*, *28*, 419–475. https://doi.org/10.1146/annurev.earth.28.1.419

Hinnov, L. A. (2018). Cyclostratigraphy and astrochronology in 2018. In: M. Montenari (Ed.), *Stratigraphy & timescales: Cyclostratigraphy and astrochronology* (pp. 1–80). Cambridge, MA: Academic Press. https://doi.org/10.1016/bs.sats.2018.08.004

Hinnov, L. A., Wu, H., & Fang, Q. (2016). Reply to the comment on "Geologic evidence for chaotic behavior of the planets and its constraints on the third-order eustatic sequences at the end of the Late Paleozoic Ice Age" by Qiang Fang, Huaichun Wu, Linda A. Hinnov, Xiuchun Jing, Xunlian Wang, and Qingchun Jiang [Palaeogeography Palaeoclimatology Palaeoecology 400 (2015) 848–859]. *Palaeogeography, Palaeoclimatology, Palaeoecology*, *461*, 475–480. https://doi.org/10.1016/j.palaeo.2016.07.030

Hocking, R. M., & Playford, P. E. (2000). Cycle types in carbonate platform facies, Devonian reef complexes, Canning Basin, Western Australia. *Geological Survey of Western Australia, Annual Review*, *2000–2001*, 74–80.

Kaufmann, B. (2006). Calibrating the Devonian Time Scale: A synthesis of U-Pb ID-TIMS ages and conodont stratigraphy. *Earth-Science Reviews.*, *76*, 175–190. https://doi.org/10.1016/j.earscirev.2006.01.001

Kemp, D. B. (2011). Shallow-water records of astronomical forcing and the eccentricity paradox. *Geology*, *39*, 491–494. https://doi.org/10.1130/G31878.1

Kemp, D. B., & Van Manen, S. M. (2019). Metre-scale cycles in shallow water carbonate successions: Milankovitch and stochastic origins. *Sedimentology*, https://doi.org/10.1111/sed.12609

Kemp, D. B., Van Manen, S. M., Pollitt, D. A., & Burgess, P. M. (2016). Investigating the preservation of orbital forcing in peritidal carbonates. *Sedimentology*, *63*, 1701–1718. https://doi.org/10.1111/sed.12282

Klapper, G. (2007). Frasnian (Upper Devonian) conodont succession at Horse Spring and correlative sections, Canning Basin, Western Australia. *Journal of Paleontology*, *81*, 513–537. https://doi.org/10.1666/05088.1

Koerschner, W. F. III, & Read, J. F. (1989). Field and modelling studies of Cambrian carbonate cycles, Virginia Appalachians. *Journal of Sedimentary Research*, *59*, 654–687. https://doi.org/10.1306/212F9048-2B24-11D7-8648000102C1865D

Königshof, P., Da Silva, A. C., Suttner, T. J., Kido, E., Waters, J., Carmichael, S. K., … Spassov, S. (2015). Shallow-water facies setting around the Kačák Event: a multidisciplinary approach. In: R. T. Becker, P. Könighsof, & C. E. Brett (Eds.), *Devonian climate, sea level and evolutionary events* (Vol. *423*, pp. 171–199). Geological Society, London, Special Publications. https://doi.org/10.1144/SP423.4

Lehrmann, D. J., & Goldhammer, R. K. (1999). Secular variation in parasequence and facies stacking patterns of platform carbonates: a guide to application of stacking pattern analysis in strata of diverse ages and settings. In: P. M. Harris, A. H. Saller, & J. A. Simo (Eds.), *Advances in carbonate sequence stratigraphy: applications to reservoirs, outcrops, and models* (Vol. *63*, pp. 187–225). SEPM Special Publication.

Machlus, M. L., Olsen, P. E., Christie-Blick, N., & Hemming, S. R. (2008). Spectral analysis of the lower Eocene Wilkins Peak Member, Green River Formation, Wyoming: Support for Milankovitch cyclicity. *Earth and Planetary Science Letters*, *268*, 64–75. https://doi.org/10.1016/j.epsl.2007.12.024

Martinez, M. (2018). Chapter four - mechanisms of preservation of the eccentricity and longer-term milankovitch cycles in detrital supply and carbonate production in hemipelagic marl-limestone alternations. In: M. Montenari (Ed.), *Stratigraphy & timescales: Cyclostratigraphy and Astrochronology* (pp. 189–218). Cambridge, MA: Academic Press. https://doi.org/10.1016/bs.sats.2018.08.002

Martinez, M., Kotov, S., De Vleeschouwer, D., Damien, P., & Pälike, H. (2016). Testing the impact of stratigraphic uncertainty on spectral analyses of sedimentary series. *Climate of the past*, *12*, 1765–1783. https://doi.org/10.5194/cp-12-1765-2016

McLean, D. J., & Mountjoy, E. W. (1994). Allocyclic control on Late Devonian buildup development, southern Canadian Rocky Mountains. *Journal of Sedimentary Research*, *64*, 326–394. https://doi.org/10.1306/D4267FBE-2B26-11D7-8648000102C1865D

Meyers, S. R. (2015). The evaluation of eccentricity-related amplitude modulation and bundling in paleoclimate data: An inverse approach for astrochronologic testing and time scale optimization. *Paleoceanography*, *30*, 1625–1640. https://doi.org/10.1002/2015PA002850

Meyers, S. R. (2019). Cyclostratigraphy and the problem of astrochronologic testing. *Earth-Science Reviews*, *190*, 190–223. https://doi.org/10.1016/j.earscirev.2018.11.015

Meyers, S. R., & Sageman, B. B. (2007). Quantification of deep-time orbital forcing by average spectral misfit. *American Journal of Science*, *307*, 773–792. https://doi.org/10.2475/05.2007.01

Meyers, S. R., Sageman, B. B., & Hinnov, L. A. (2001). Integrated quantitative stratigraphy of the Cenomanian-Turonian Bridge Creek Limestone Member using evolutive harmonic analysis and stratigraphic modeling. *Journal of Sedimentary Research*, *71*, 628–644. https://doi.org/10.1306/012401710628

Miall, A. D. (1973). Markov chain analysis applied to an ancient alluvial plain succession. *Sedimentology*, *20*, 347–364. https://doi.org/10.1111/j.1365-3091.1973.tb01615.x

Ndiaye, M. A. (2007a). A multipurpose software for stratigraphic signal analysis. Ph.D. Thesis. Université de Genève, Département de Géologie et Paléontologie, 118 p.

Ndiaye, M. A. (2007b). *Multipurpose software for stratigraphic signal analysis (version 1.0.4)*. Retrieved from http://home.etu.unige.ch/~ndiayma8/

Osleger, D. (1991). Subtidal carbonate cycles: Implications for allocyclic vs. autocyclic controls. *Geology*, *19*, 917–920. https://doi.org/10.1130/0091-7613(1991)019%3C0917:SCCIFA%3E2.3.CO;2

Pas, D., Hinnov, L., Day, J. E., Kodama, K., Sinnesael, M., & Liu, W. (2018). Cyclostratigraphic calibration of the Famennian stage (Late Devonian, Illinois Basin, USA). *Earth and Planetary Science Letters*, *488*, 102–114. https://doi.org/10.1016/j.epsl.2018.02.010

Peterhänsel, A., & Egenhoff, S. O. (2008) Lateral variabilities of cycle stacking patterns in the Latemar, Triassic, Italian Dolomites. In: J. Lukasik, & J. A. Simo (Ed.), *Controls on carbonate platform and reef development* (Vol. *89* pp. 217–229), SEPM Special Publication. https://doi.org/10.2110/pec.08.89.0217

Playford, P. E. (1980). Devonian "Great Barrier Reef" of Canning Basin, Western Australia. *AAPG Bulletin*, *64*, 814–840. https://doi.org/10.1306/2F9193BE-16CE-11D7-8645000102C1865D

Playford, P. E., Hocking, R. M., & Cockbain, A. E. (2009). Devonian reef complexes of the Canning Basin, Western Australia. *Bulletin of the Geological Survey of. Western Australia*, *145*, 444. https://doi.org/10.2110/sepmsp.106.05

Playford, P. E., Hurley, N. F., Kerans, C., & Middleton, M. F. (1989). Reefal platform development, Devonian of the Canning Basin, Western Australia. In: P. D. Crevello, J. L. Wilson, J. F. Sarg, & J. F. Read (Eds.), *Controls on carbonate platform and basin development* (Vol. *44*, pp. 187–202). SEPM Special Publication. https://doi.org/10.2110/pec.89.44.0187

Playton, T. E., Hocking, R. M., Tohver, E., Hillbun, K., Haines, P. W., & Trinajstic, K. … Wray, D. (2016). Integrated stratigraphic correlation of Upper Devonian platform-to-basin carbonate sequences, Lennard Shelf, Canning Basin, Western Australia: advances in carbonate margin-to-slope sequence stratigraphy and stacking patterns. In: T. E. Playton, C. Kerans, & J. A. W. Weissenberger (Eds), *New advances in Devonian carbonates: outcrop analogs, reservoirs, and chronostratigraphy* (Vol. *107*, 248–301). SEPM Special Publication. https://doi.org/10.2110/sepmsp.107.10

Playton, T. E., & Kerans, C. (2015). Late Devonian carbonate margins and foreslopes of the Lennard Shelf, Canning Basin, Western Australia, part A: Development during backstepping and the aggradation-to-progradation transition. *Journal of Sedimentary Research*, *85*, 1334–1361. https://doi.org/10.2110/jsr.2015.84

Pollitt, D. A., Burgess, P. M., & Wright, V. P. (2014). Investigating the occurrence of hierarchies of cyclicity in platform carbonates. In: D. G. Smith, R. J. Bailey, P. M. Burgess, & A. J. Fraser (Eds.), *Strata and Time: Probing the Gaps in Our Understanding* (Vol. *404*,

pp. 123–150). Geological Society, London, Special Publications. https://doi.org/10.1144/SP404.3

Powers, D. W., & Easterling, R. G. (1982). Improved methodology for using embedded Markov chains to describe cyclical sediments. *Journal of Sedimentary Petrology*, *52*, 913–923. https://doi.org/10.1306/212F808F-2B24-11D7-8648000102C1865D

Pratt, B. R., & James, N. P. (1986). The St George Group (Lower Ordovician) of western Newfoundland: Tidal flat island model for carbonate sedimentation in shallow epeiric seas. *Sedimentology*, *33*, 313–343. https://doi.org/10.1111/j.1365-3091.1986.tb00540.x

Prokoph, A., & Agterberg, F. P. (1999). Detection of sedimentary cyclicity and stratigraphic completeness by wavelet analysis: An application to late Albian cyclostratigraphy of the western Canada sedimentary basin. *Journal of Sedimentary Research*, *69*, 862–875. https://doi.org/10.2110/jsr.69.862

Rankey, E. C. (2002). Spatial patterns of sediment accumulation on a Holocene carbonate tidal flat, northwest Andros Island, Bahamas. *Journal of Sedimentary Research*, *72*, 591–601. https://doi.org/10.1306/020702720591

Read, J. F. (1973). Carbonate cycles, Pillara Formation (Devonian), Canning Basin, Western Australia. *Bulletin of Canadian Petroleum Geology*, *21*, 38–51. https://doi.org/10.35767/gscpgbull.21.1.038

Read, J. F., Osleger, D., & Elrick, M. (1991). Two-dimensional modeling of carbonate ramp sequences and component cycles. In: E. K. Franseen, W. L. Watney, C. G. St. Kendall, & W. Ross (Eds.), *Sedimentary modeling: Computer simulations and methods for improved parameter definition*. (Vol. *233*, pp. 473–488). Kansas Geological Survey Bulletin.

Riquier, L., Averbuch, O., Devleeschouwer, X., & Tribovillard, N. (2010). Diagenetic versus detrital origin of the magnetic susceptibility variations in some carbonate Frasnian-Famennian boundary sections from Northern Africa and Western Europe: Implications for paleoenvironmental reconstructions. *International Journal of Earth Sciences*, *99*, 57–73. https://doi.org/10.1007/s00531-009-0492-7

Rothman, D. H., & Grotzinger, J. P. (1995). Scaling properties of gravity-driven sediments. *Nonlinear Processes in Geophysics*, *2*, 178–185. https://doi.org/10.5194/npg-2-178-1995

Samankassou, E., & Enos, P. (2019). Lateral facies variations in the Triassic Dachstein platform: A challenge for cyclostratigraphy. *The Depositional Record*, *5*, 469–485. https://doi.org/10.1002/dep2.80

Sardar Abadi, A., Da Silva, A. C., Amini, A., Boulvain, F., Sardar Abadi, M. H., & Aliabadi, A. A. (2014). Tectonically-controlled sedimentation: Impact on sediment supply and basin evolution during the Middle Jurassic Kashafrud Formation, Kopeh-Dagh Basin, northeast Iran. *International Journal of Earth Sciences*, *103*, 2233–2254. https://doi.org/10.1007/s00531-014-1041-6

Schlager, W. (2005). *Carbonate Sedimentology and Sequence Stratigraphy. Concepts in Sedimentology and Paleontology* (Vol. *8*, 200 p.). SEPM. https://doi.org/10.2110/csp.05.08

Schwarzacher, W. (2000). Repetitions and cycles in stratigraphy. *Earth-Science Reviews*, *50*, 51–75. https://doi.org/10.1016/S0012-8252(99)00070-7

Śliwiński, M. G., Whalen, M. T., Meyer, F. J., & Majs, F. (2012). Constraining clastic input controls on magnetic susceptibility and trace element anomalies during the Late Devonian *punctata* Event in the Western Canada Sedimentary Basin. *Terra Nova*, *24*, 301–309. https://doi.org/10.1111/j.1365-3121.2012.01063.x

Smith, D. G. (2019). Millennial-scale climate changes manifest Milankovitch combination tones and Hallstatt solar cycles in the Devonian greenhouse world: Comment. *Geology*, *47*, e488–e488. https://doi.org/10.1130/G46475C.1

Southgate, P. N., Kennard, J. M., Jackson, M. J., O'Brien, P. E., & Sexton, M. J. (1993). Reciprocal lowstand clastic and highstand carbonate sedimentation, subsurface Devonian reef complex, Canning Basin, Western Australia. In: R. G. Loucks, & J. F. Sarg (Eds.), *Carbonate sequence stratigraphy* (Vol. *57*, pp. 157–179). AAPG Memoir. https://doi.org/10.1306/M57579C6

Strasser, A. (2018). Cyclostratigraphy of shallow-marine carbonates: limitations and opportunities. In: M. Montenari (Ed.), *Stratigraphy & timescales: cyclostratigraphy and astrochronology* (pp. 151–187). Cambridge, MA: Academic Press. https://doi.org/10.1016/bs.sats.2018.07.001

Tucker, M., & Garland, J. (2010). High-frequency cycles and their sequence stratigraphic context: Orbital forcing and tectonic controls on Devonian cyclicity, Belgium (The André Dumont medallist lecture). *Geologica Belgica*, *13*, 213–240.

Türk, G. (1979). Transition analysis of structural sequences: Discussion. *Geological Society of America Bulletin*, *90*, 989–991. https://doi.org/10.1130/0016-7606(1979)90%3C989:TAOSSD%3E2.0.CO;2

Ward, B. W. (1999). Tectonic control on backstepping sequences revealed by mapping of Frasnian backstepped platforms, Devonian reef complexes, Napier Range, Canning Basin, Western Australia. In: P. M. Harris, A. H. Saller, & J. A. Simo (Eds.), *Advances in carbonate sequence stratigraphy: application to reservoirs, outcrops, and models* (Vol. *63*, pp. 47–74). SEPM Special Publication. https://doi.org/10.2110/pec.99.11.0047

Weedon, G. P. (2003). *Time-series analysis and cyclostratigraphy: Examining stratigraphic records of environmental cycles*, Cambridge: Cambridge University Press.

Weij, R., Reijmer, J. J. G., Eberli, G. P., & Swart, P. K. (2018). The limited link between accommodation space, sediment thickness, and inner platform facies distribution (Holocene-Pleistocene, Bahamas). *The Depositional Record*, *5*, 400–420. https://doi.org/10.1002/dep2.50

Westphal, H., Hilgen, F., & Munnecke, A. (2010). An assessment of the suitability of individual rhythmic carbonate successions for astrochronological application. *Earth-Science Reviews*, *99*, 19–30. https://doi.org/10.1016/j.earscirev.2010.02.001

Whalen, M. T., & Day, J. E. (2008). Magnetic susceptibility, biostratigraphy, and sequence stratigraphy: Insights into Devonian carbonate platform development and basin infilling, Western Alberta. In: J. Lukasik, & J. A. Simo (Eds.), *Controls on carbonate platform and reef development* (Vol. *89*, pp. 291–314). Society of Sedimentary Geology, Special Publication. https://doi.org/10.2110/pec.08.89.0291

Whalen, M. T., & Day, J. (2010). Cross-basin variations in magnetic susceptibility influenced by changing sea level, paleogeography, and paleoclimate: Upper Devonian, Western Canada. *Journal of Sedimentary Research*, *80*, 1109–1127. https://doi.org/10.2110/jsr.2010.093

Wilkinson, B. H., Drummond, C. N., Diedrich, N. W., & Rothman, E. D. (1999). Poisson processes of carbonate accumulation on Paleozoic and Holocene platforms. *Journal of Sedimentary Research*, *69*, 338–350. https://doi.org/10.2110/jsr.69.338

Wilkinson, B. H., Drummond, C. N., Rothman, E. D., & Diedrich, N. W. (1997). Stratal order in peritidal carbonate sequences. *Journal of Sedimentary Research*, *67*, 1068–1082. https://doi.org/10.1306/D42686CB-2B26-11D7-8648000102C1865D

Xu, H., & Maccarthy, I. A. J. (1998). Markov chain analysis of vertical facies sequences using a computer software package (SAVFS): Courtmacsherry Formation (Tournaisian), Southern Ireland. *Computers & Geosciences*, *24*, 131–139. https://doi.org/10.1016/S0098-3004(97)00086-1

SUPPORTING INFORMATION

Additional supporting information may be found online in the Supporting Information section.

How to cite this article: Ferguson IJ, Da Silva A-C, Chow N, George AD. Interplay of eustatic, tectonic and autogenic controls on a Late Devonian carbonate platform, northern Canning Basin, Australia. *Basin Res*. 2020;00:1–30. https://doi.org/10.1111/bre.12468